



**Renata Ferreira Leite Considera**

**Search for axion-like particles in ultraperipheral  
PbPb collisions at the LHCb experiment**

**Dissertação de Mestrado**

Dissertation presented to the Programa de Pós-graduação em Física of PUC-Rio in partial fulfillment of the requirements for the degree of Mestre em Física.

Advisor : Profa. Carla Göbel Burlamaqui de Mello  
Co-advisor: Prof. Murilo Santana Rangel

Rio de Janeiro  
September 2024



**Renata Ferreira Leite Considera**

**Search for axion-like particles in ultraperipheral  
PbPb collisions at the LHCb experiment**

Dissertation presented to the Programa de Pós-graduação em Física of PUC-Rio in partial fulfillment of the requirements for the degree of Mestre em Física. Approved by the Examination Committee:

**Profa. Carla Göbel Burlamaqui de Mello**

Advisor

Departamento de Física – PUC-Rio

**Prof. Murilo Santana Rangel**

UFRJ

**Profa. Marisilvia Donadelli**

UERJ

**Prof. Gero Arthur Hubertus Thilo Freiherr von Gersdorff**

Departamento de Física – PUC-Rio

Rio de Janeiro, September 20th, 2024

All rights reserved.

### **Renata Ferreira Leite Considera**

The author obtained the degree of Bachelor in Physics in 2022 from Universidade Federal Fluminense (UFF).

#### Bibliographic data

Considera, Renata

Search for axion-like particles in ultraperipheral PbPb collisions at the LHCb experiment / Renata Ferreira Leite Considera; advisor: Carla Göbel Burlamaqui de Mello; co-advisor: Murilo Santana Rangel. – 2024.

71 f: il. color. ; 30 cm

Dissertação (mestrado) - Pontifícia Universidade Católica do Rio de Janeiro, Departamento de Física, 2024.

Inclui bibliografia

1. Física – Teses. 2. axions. 3. ALPs. 4. além do Modelo Padrão. 5. Problema da CP forte. 6. Experimento LHCb. 7. Acoplamento ALP-fóton. 8. íons pesados. I. Göbel, Carla. II. Santana Rangel, Murilo. III. Pontifícia Universidade Católica do Rio de Janeiro. Departamento de Física. IV. Título.

CDD: 530

## Acknowledgments

Firstly, I would like to thank God for His daily mercies, for granting me the strength to complete this work, and for blessing me with incredible people whose support, guidance, and encouragement have been essential throughout this journey.

I am deeply grateful to my advisor, Carla Göbel, for accepting me as her student, for her insightful guidance, and for her endless patience in explaining the same things to me countless times. Your dedication and encouragement have been crucial to my growth and the completion of this dissertation.

I would also like to thank my co-advisor, Murilo Rangel, for his invaluable advices, for always ensuring that I truly understood the key concepts of this work, and for his kindness during this process.

Then I wish to thank my family. My parents, Sergio and Jô, for their emotional and financial support and for always being proud of my achievements. To my sister Carol and my brother Matheus, thank you for your constant support and for always being there for me. And to my nephews Wallace and Pedro, you are the true joys of my life.

To the best friends life could have given me—Aimy, Débora, and Nico—thank you so much for your long-term friendship, for being present at every step of my life, for the fun times, the nearly free therapy sessions, and all your love and support.

To Karolayne, thank you for your partnership over these past years, ever since our undergraduate days. Thank you for your patience in listening to my long voice messages (almost like podcasts), for always checking in on me, and for offering help even when I take ages to respond. Thank you for sharing your journey with me as well—I'm certain you will be a very successful researcher.

Last but definitely not least, my gratitude goes to André, my husband, who has been there to listen to all my complaints and tears throughout this period—sorry for that! Your support has helped me realize that life is so much more than just this. Thank you for helping me find my way during this time when I often felt lost. Thank you also for being willing to watch all the slasher film franchises with me, for introducing me to so much wonderful music, and for the "Tem café!" every morning. I am incredibly grateful to share this life with you. *Moi je suis né ici pour n'être qu'avec toi...* one day, we'll finish that online French course.

This study was financed in part by the Coordenação de Aperfeiçoamento de Pessoal de Nível Superior - Brasil (CAPES) - Finance Code 001.

## Abstract

Considera, Renata; Göbel, Carla (Advisor); Santana Rangel, Murilo (Co-Advisor). **Search for axion-like particles in ultraperipheral PbPb collisions at the LHCb experiment.** Rio de Janeiro, 2024. 71p. Dissertação de Mestrado – Departamento de Física, Pontifícia Universidade Católica do Rio de Janeiro.

The Standard Model (SM) of particle physics is currently the most accepted theory for describing the fundamental interactions among elementary particles. However, the model alone fails to explain several phenomena, from neutrino oscillations to dark matter. One current puzzle of the SM is the so-called strong CP problem. Although Charge-Parity (CP) symmetry is known to be violated by the weak interactions, it is conserved by the strong interaction to a high precision. Nevertheless, the SM Lagrangian has a term that could allow strong-induced CP violation, and only an extreme fine-tuning would prevent this effect. The solution could come with the introduction of a new particle, the axion. This idea was later generalized into a broader class of particles known as axion-like particles (ALPs). Despite extensive searches, no evidence of ALPs has been observed so far, with only upper limits on their coupling constants being reported.

This dissertation describes the search for ALPs decaying into a pair of photons in ultraperipheral PbPb collisions at a center-of-mass energy of 5.02 TeV. The data corresponds to an integrated luminosity of  $0.2 \text{ nb}^{-1}$ , collected by the LHCb experiment. The forward configuration of the LHCb detector is well-suited for investigating low-mass ALPs, a challenging range for other detectors. Photon candidates are reconstructed and identified using information from the electromagnetic calorimeter. Our analysis covers an ALP mass range from 3 to 10 GeV and ALP-photon couplings from  $10^{-1}$  to  $1 \text{ TeV}^{-1}$ . Although our exclusion region is small and overlaps with recent analyses, this study demonstrates the potential, in run 3 and beyond, for LHCb to contribute to ALP searches in ultraperipheral collisions.

## Keywords

axions; ALPS; beyond the Standard Model; Strong CP problem; LHCb experiment; ALP-photon coupling; heavy ions.

## Resumo

Considera, Renata; Göbel, Carla; Santana Rangel, Murilo. **Busca por partículas tipo áxion em colisões PbPb ultraperiféricas no experimento LHCb**. Rio de Janeiro, 2024. 71p. Dissertação de Mestrado – Departamento de Física, Pontifícia Universidade Católica do Rio de Janeiro.

O Modelo Padrão (MP) da física de partículas é atualmente a teoria mais aceita para descrever as interações fundamentais entre partículas elementares. No entanto, o modelo por si só não consegue explicar vários fenômenos, desde oscilações de neutrinos até matéria escura. Um enigma atual do MP é o chamado problema de CP forte. Embora se saiba que a simetria de Carga-Paridade (CP) é violada pelas interações fracas, ela é conservada pela interação forte com alta precisão. No entanto, a Lagrangeana do MP tem um termo que poderia permitir violação de CP induzida por interação forte, e apenas um extremo ajuste fino evitaria esse efeito. A solução poderia vir com a introdução de uma nova partícula, o áxion. Esta ideia foi posteriormente generalizada para uma classe mais ampla de partículas conhecidas como partículas tipo áxions (ALPs). Apesar de extensas pesquisas, nenhuma evidência de ALPs foi observada até hoje, sendo relatados apenas limites superiores em suas constantes de acoplamento.

Esta dissertação descreve a busca por ALPs decaindo em um par de fótons em colisões ultraperiféricas de PbPb a uma energia de centro de massa de 5,02 TeV. Os dados correspondem a uma luminosidade integrada de 0,2 nb<sup>-1</sup>, coletados pelo experimento LHCb. A configuração frontal do detector LHCb é adequada para investigar ALPs de baixa massa, uma faixa desafiadora para outros detectores. Os candidatos a fótons são reconstruídos e identificados usando informações do calorímetro eletromagnético. Esta análise cobre uma faixa de massa de ALP de 3 a 10 GeV e acoplamentos de ALP-fótons de 10<sup>-1</sup> a 1 TeV<sup>-1</sup>. Embora a região de exclusão obtida seja pequena e se sobreponha a análises recentes, este estudo demonstra o potencial, no run 3 e além, do experimento LHCb para contribuir em pesquisas de ALP em colisões ultraperiféricas.

### Palavras-chave

axions; ALPs; além do Modelo Padrão; Problema da CP forte; Experimento LHCb; Acoplamento ALP-fóton; íons pesados.

# Table of contents

<b>1</b>	<b>Introduction</b>	<b>13</b>
<b>2</b>	<b>Theoretical Aspects</b>	<b>15</b>
2.1	The Standard Model	15
2.2	The Strong CP problem and axion-like particles (ALPs)	19
2.3	Searching for ALPs	21
2.3.1	Ultrapерipheral collisions (UPC)	22
2.3.2	Current status of ALPs searches	24
<b>3</b>	<b>The LHC and the LHCb experiment</b>	<b>28</b>
3.1	The LHC	28
3.2	The LHCb detector during Run 2	30
3.2.1	Tracking system	31
3.2.2	Particle identification	33
3.2.3	Trigger and acquisition	36
3.2.4	HeRSChel detector	38
<b>4</b>	<b>Analysis of ALP searches at LHCb during Run 2</b>	<b>40</b>
4.1	Analysis Strategy	40
4.1.1	Setting upper limits with the $CLs$ method	41
4.1.2	Definition of variables	46
4.2	Analysis samples and selection	48
4.2.1	Data sample	48
4.2.2	Monte Carlo simulation samples	49
4.2.3	Selection	50
4.2.4	Trigger and HeRSChel Efficiencies	54
4.3	Signal and Background estimations	55
4.3.1	MC ALP signal yield	55
4.3.2	Light-by-Light background	56
4.3.3	Dielectron background	57
4.4	Results and Discussion	62
4.4.1	Expected $CLs$ limits	62
4.4.2	Exclusion Region	63
<b>5</b>	<b>Conclusions and Future Prospects</b>	<b>65</b>
<b>6</b>	<b>Bibliography</b>	<b>67</b>

## List of figures

Figure 2.1	Schematic representation of the elementary particles of the Standard Model: the twelve fundamental fermions and the five gauge bosons are shown along with its antiparticles and the Higgs boson.	17
Figure 2.2	Schematic diagram of an UPC of two ions, where $Z$ is the atomic number and the impact parameter, $b$ , is larger than the sum of the two radii, $R_A + R_B$ [1].	23
Figure 2.3	Representation of diphoton production in PbPb or pPb collisions by (a) the $\gamma\gamma \rightarrow a \rightarrow \gamma\gamma$ subprocess and (b) Light-by-Light scattering. (c) The dielectron production, which is an important background when the electrons are misidentified as photons. $S_{abs}^2$ is the absorptive factor, and it depends on the impact parameter, $b$ , of the PbPb collision [2].	24
Figure 2.4	Current limits on the ALP-photon coupling vs. ALP mass from cosmological, astrophysical, and accelerator searches [3].	25
Figure 2.5	Detailed bounds in the $(m_a, g_{a\gamma})$ plane from all existing accelerator and collider ALP searches for masses $m_a \approx 1 \text{ MeV} - 3 \text{ TeV}$ [3].	26
Figure 2.6	Representative diagrams of ALPs searches at the LHC via exclusive diphotons (topleft), diphotons from vector-boson-fusion (with $V = \gamma, Z$ , top right), exotic triphoton Z-boson decays (bottom left), and exotic 4-photon Higgs-boson decays (bottom right) [3].	26
Figure 2.7	Expected sensitivity to the ALP production in PbPb ultraperipheral collision. "This work" refers to [2].	27
Figure 3.1	The LHC underneath the French-Swiss border, near Geneva.	28
Figure 3.2	CERN's accelerator complex.	29
Figure 3.3	Schematic overview of the LHCb detector layout during the Run 1 and Run 2 data takings. Taken from [4].	30
Figure 3.4	Strength of the magnet field component $B_y$ as a function of the $z$ coordinate in the different tracking detectors of LHCb and overview of the track types reconstructed in the LHCb. Taken from [5]	32
Figure 3.5	Layout of the calorimeter system. Taken from [4].	34
Figure 3.7	Sketch of the expected energy deposition in the various subdetectors of the calorimeter system by different species of particles. Taken from [6]	35
Figure 3.6	Calorimeter cells segmentation of the SPD, PS, and ECAL (left), and the HCAL (right). Taken from [4].	35
Figure 3.8	Stages of the LHCb trigger system and their event rates during Run 2.	37
Figure 3.9	Schematic view of the HeRSChEL stations around the LHCb interaction point, where for illustration the HeRSChEL stations have been magnified by a factor of 20 with respect to the rest of the LHCb detector. The $z$ -axis is not to scale. Image adapted from [7].	39

- Figure 4.1 Feynman diagrams for possible interactions in ultraperipheral PbPb collisions at the LHCb. Left: diphoton production in a LbL scattering. Right: QED dielectron production. A potential electromagnetic excitation of the outgoing Pb ions is denoted by (\*). Taken from [8]. 41
- Figure 4.2 The  $CL_{s+b}$  curve for 1000 values of  $s + b$  between 0 and 10. At  $s + b = 7.75$ , the probability of observing  $n_{obs} = 3$  events or less is 5%. At this point, we can get the  $s_{up}$  from the subtraction of the given background. 45
- Figure 4.3 Confidence levels  $CL_{s+b}$  and  $CL_s$  for the observed number of events. 46
- Figure 4.4 Feynman diagram of ALP production and decay in ultraperipheral PbPb collisions [9]. 47
- Figure 4.5 From top-left to bottom-right: number of photons, pseudorapidity, acoplanarity and diphoton  $p_T^2$  for dielectron (line-pink) and 3 GeV ALP (filled-blue) simulation samples. The requirements are explained in the text. 51
- Figure 4.6 Punzi FoM for acoplanarity ( $A_\phi$ ) and diphoton transverse momentum squared ( $p_T^2(\gamma\gamma)$ ) with  $a = 3$  (top) and  $a = 5$  (bottom). 52
- Figure 4.7 Signal efficiencies for different selection values of acoplanarity (left), diphoton transverse momentum squared (middle), and the combination of both (right) 53
- Figure 4.8 From top-left to bottom-right:  $n_{VELOtracks}$ , diphoton mass, photon's  $p_T$  distributions for dielectron (line-pink) and 3 GeV ALP (filled-blue) simulation samples. The requirements are explained in the text. 53
- Figure 4.9 Efficiency results as a function of transverse momentum using the tag-and-probe method based on the decays of  $\eta$  and  $\pi^0$  resonances to pairs of photons. 54
- Figure 4.10 Distribution for the HeRSChel variable for data,  $\log(\chi_{HRC}^2)$ . The green line represents the cut in 8.35 considered for calculate the HeRSChel efficiency. The selection criteria for this sample is the same as in table 4.2, including the L0PhotonLowMult trigger requirements and  $n_{VELOtracks} \geq 1$ . 55
- Figure 4.11 Distribution of the number of VELO tracks (left) and the number of photons (right) for the dielectron control sample. 58
- Figure 4.12 Distributions of the photon transverse momentum ( $p_T$ ) for both photons, and the diphoton invariant mass (top right) in the dielectron control sample. The bottom row shows the same distributions without the  $n_{photons} = 2$  requirement. 59
- Figure 4.13 Distributions of the diphoton acoplanarity (left) and the diphoton transverse momentum squared ( $p_T^2$ ) (right) in the dielectron control sample. The bottom row shows the same distributions without the  $n_{photons} = 2$  requirement. 59
- Figure 4.14 Distributions of the pseudorapidity for the leading photon (left) and subleading photon (right) in the dielectron control sample. The bottom row shows the same distributions without the  $n_{photons} = 2$  requirement. 60
- Figure 4.15 Distributions of the azimuthal angle for the leading photon (left) and subleading photon (right) in the dielectron control sample. The bottom row shows the same distributions without the  $n_{photons} = 2$  requirement. 60

Figure 4.16 Shape comparison between two different selections for the dielectron simulation. As explained in the text,  $n_{VELOtracks} = 1$  or 3 or 4 (blue points) and  $n_{VELOtracks} = 2$  (filled-green) have similar shapes. The bottom plot exclude the  $n_{photons} = 2$  and  $p_T^2(\gamma\gamma) > 0.03 \text{ GeV}^2$  criteria in order to enhance the statistics. 61

Figure 4.17 Diphoton invariant mass distribution for the ALP signal with mass hypotheses of 3 GeV (left) and 5 GeV (right). The distributions combine the expected ALP signal with background contributions. 62

Figure 4.18  $CLs$  limits for ALP mass hypotheses of 3 GeV (left) and 5 GeV (right) using the TLimit class from the ROOT framework. These curves show the expected exclusion limits for the ALP-photon coupling constant at 95% CL (light pink dashed line). 63

Figure 4.19 Exclusion region in the  $g_{a\gamma}$  versus ALP mass plane, representing the values excluded at 95% CL for the tested mass range, compared with the exclusion limits obtained by ATLAS [9] and CMS [8] experiments. 64

Figure 5.1 Left: Acoplanarity of the photon pairs. Right: Leading photon  $E_T$  photon pairs. Both for data taken in 2018 and 2023. In 2018, the photon pairs are selected with a hardware trigger while for 2023 data set, they are selected with a software trigger implemented in GPUs. Taken from ref [10] 66

## List of tables

Table 4.1	Trigger and stripping lines requirements	49
Table 4.2	Selection criteria for the diphoton candidates	54
Table 4.3	Expected number of ALP candidates ( $n_{exp}$ ) for different mass hypotheses, after applying the selection criteria. The table also shows the predicted cross-sections ( $\sigma_{\gamma\gamma\rightarrow a\rightarrow\gamma\gamma}$ ) [11], the number of generated events ( $n_{gen,ALP}$ ), and the number of events remaining after the selection ( $n_{sel}$ ).	56
Table 4.4	Upper limits on the ALP-photon coupling constant $g_{a\gamma}$ for different ALP mass hypotheses, calculated using the $CLs$ method. These limits do not account for systematic uncertainties.	63

*Andrew Largeman: Hey Albert.*

*Albert: Yeah?*

*Andrew Largeman: Good luck exploring the  
infinite abyss.*

*Albert: Thank you, and hey, you too.*

**Zach Braff as Andrew Largeman, *Garden State*.**

# 1

## Introduction

The Standard Model (SM) of particle physics successfully describes three of the four fundamental forces in nature—electromagnetic, strong, and weak interactions—along with all known elementary particles. Despite its success, the SM is not believed to be complete. As indicated by various experimental observations, there are still several key aspects of the universe that remain unexplained, such as dark matter, dark energy [12, 13], neutrino oscillations [14], and the matter-antimatter asymmetry [15, 16].

One of the unresolved aspects in the SM is the so-called strong CP problem, which concerns the absence of any violation of charge-parity (CP) symmetry in strong interactions. According to quantum chromodynamics (QCD), the theory describing strong interactions, there could be a term in the QCD Lagrangian that allows for CP violation [17]. However, experiments have not observed such violations, leading to an unnaturally small value for the strong CP-violating parameter,  $\theta$ . This is known as the strong CP problem. The introduction of a hypothetical particle called axion was initially proposed as a solution [18, 19]. Axions dynamically cancel out the CP-violating effects, providing a natural explanation for the smallness of  $\theta$ . This idea has been generalized into a broader class of particles known as axion-like particles (ALPs).

Axions and ALPs share similar properties, but ALPs are not restricted to solving the strong CP problem. Instead, they arise in many theories beyond the SM. ALPs can have a wide range of masses and couplings, making them versatile candidates for new physics. They can interact with photons, gluons, and other particles, and their observation would provide crucial insights into the nature of fundamental interactions and the structure of the universe.

Despite extensive theoretical motivation and experimental efforts, no evidence for ALPs has been observed so far. Searches for ALPs have been conducted in various experimental settings, including laboratory-based experiments, astrophysical observations, and collider experiments. The latter, such as those conducted at the Large Hadron Collider (LHC), offer a unique environment to produce and detect ALPs due to the high energy and luminosity of the collisions. These experiments aim to explore a wide range of ALP masses and couplings, providing stringent constraints on their properties [3, 20].

This dissertation describes the analysis performed to search for hypothetical ALPs that couple only with photons, using data collected by the LHCb

experiment during Run 2, between November and December of 2018, from ultraperipheral PbPb collisions. These collisions, characterized by impact parameters larger than twice the nuclear radius, allow ions to interact via their clouds of virtual photons, making them ideal for studying ALPs with photon couplings. Additionally, as a forward detector, the LHCb detector is well-suited for investigating low-mass ALPs ( $m_a < 10$  GeV), a mass range that is challenging for other detectors due to limitations in photon reconstruction [1, 21].

This document is organized as follows. In Chapter 2, we provide a brief overview of the SM and some of its unanswered features, particularly the strong CP problem, and how the introduction of the axion could solve it. Then, we present some potential methods for producing and detecting ALPs, highlighting the current status of their searches. In Chapter 3, a description of the LHC and the LHCb experiment is given, with special emphasis placed on the most relevant subsystems used for this analysis. Chapter 4 presents the strategy and results of our analysis. We begin by introducing essential statistical concepts necessary for interpreting searches with limited statistics, with a particular focus on the  $CL_s$  method for setting upper limits, followed by a detailed explanation of the analysis steps, including the description of the relevant kinematic variables and the requirements used to remove specific background contributions in the selection process. To ensure the integrity of the analysis and avoid potential biases, a blinded analysis is employed, meaning that the data in the signal region is not examined until the analysis procedure is finalized. Finally, we present the exclusion region in the  $(g_{a\gamma}, \text{mass})$  parameter space, calculated based on the expected background levels. As this is a blinded analysis, the results outline the methodology and strategy that will be used to obtain the final results once the data is unblinded. The conclusions of this dissertation are presented in Chapter 5.

## 2 Theoretical Aspects

This chapter provides a brief overview of the Standard Model (SM) of particle physics and some of its not fully understood features, particularly the strong CP problem, and how the introduction of a new particle, the axion, could solve it. Then, we present some potential methods for producing and detecting axion-like particles (ALPs), highlighting the current status of ALPs searches.

### 2.1 The Standard Model

The Standard Model is currently the most accepted theory that describes the elementary particles and how they interact through three of the fundamental forces:<sup>1</sup> electromagnetic, strong and weak.

Fermions are the building blocks of matter, so we call them the *matter particles*, they are spin  $\frac{1}{2}$  particles and are divided into quarks and leptons. The electron, the electron neutrino, the up-quark and down-quark are known as the first-generation fermions. For each of the four first-generation particles, there are two copies which differ only in their masses, they are known as the second and third generations. There is the muon ( $\approx 200$  times the electron mass) as a second-generation electron and the tau ( $\approx 3500$  the electron mass) as the third-generation one. For the up-quark (down-quark), there are the charm-quark (strange-quark) in the second-generation and the top-quark (bottom or beauty -quark) in the third. As for the electron neutrino, there are two more copies of it: the muon neutrino (second-generation) and the tau neutrino (third-generation). Although it is known that neutrinos possess mass, their masses are so small that they have not yet been individually measured. All these twelve matter particles, as free fields, are described by the Dirac equation:

$$(i\gamma^\mu\partial_\mu - m)\psi = 0, \tag{2-1}$$

where  $\mu$  can take the values 0, 1, 2 and 3. The first term inside the parenthesis,  $i\gamma^\mu\partial_\mu$ , represents the momentum operator acting on the wavefunction of the particle,  $\psi$ , and  $m$  is the mass of the particle. One of the implications of the Dirac equation is the existence of an antiparticle state for each fermion. The antiparticles have the exact same mass and lifetime as their particle counterparts but with opposite additive charges.

---

<sup>1</sup>The SM doesn't describe gravity.

All observable matter, including ourselves, is composed of the first-generation fermions: up-quarks, down-quarks and electrons. The remaining particles, the ones that belong to higher generations, are unstable and eventually decay into the first-generation fermions.

The forces are carried out by boson fields, with integer spin, mediating the interactions between the matter particles. As mentioned before, the SM specifies three of the fundamental interactions in nature: electromagnetic, strong and weak. Each of these forces is expressed by a Quantum Field Theory (QFT), where a force is described in terms of the exchange of a particle, a gauge boson. For electromagnetism, this corresponds to the theory of Quantum Electrodynamics (QED), where interactions among charged particles occur through the exchange of photons. The strong interaction is governed by Quantum Chromodynamics (QCD) and has the gluons as its force carrying particle. In the case of the weak force, the interaction is mediated by the  $W^\pm$  and  $Z^0$  bosons. Both the gluon and the photon are massless particles, while the  $W^\pm$  and  $Z^0$  bosons are massive. There is also the Higgs boson, which was discovered in 2012 by ATLAS [22] and CMS [23] experiments at the *Conseil Européen pour la Recherche Nucléaire* (CERN)'s Large Hadron Collider (LHC). With a spin zero and a mass of approximately 125 GeV, the Higgs field is responsible for providing the mechanism by which all other particles obtain mass [24].

In Fig.2.1 we have a schematic view of the elementary particles described by the SM, where we can see some more information of them.

All fermions experiment the weak force by exchanging  $W^\pm$  and  $Z^0$  bosons. The electrically charged fermions participate in the electromagnetic interaction of QED, exchanging photons. Among them, only quarks carry the QCD charge, referred to as color charge (red, green or blue),<sup>2</sup> and as a result, are influenced by the strong force, via gluons.<sup>3</sup> Due to the nature of the QCD interaction, quarks are never observed free, instead they are confined within bound states: the hadrons, ensuring that the resulting color charge is neutral (color singlet state). Hadrons are divided into baryons (formed by three quarks or three antiquarks) and mesons (one quark and one antiquark).<sup>4</sup>

---

<sup>2</sup>For antiquarks we have anti-red, anti-green and anti-blue.

<sup>3</sup>Unlike other force carriers, gluons carry a color charge and an anti-color charge, making them subject to the strong force they mediate.

<sup>4</sup>In recent years, other configurations have been discovered, such as tetraquarks (two quarks and two antiquarks) and pentaquarks (four quarks and one antiquark). These also form color neutral singlet states.

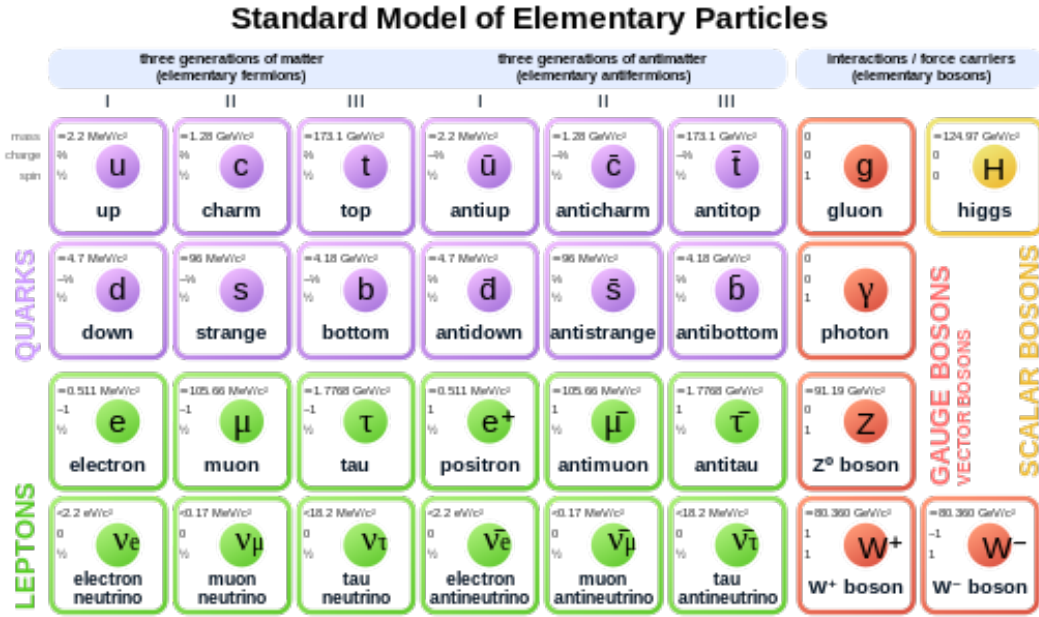


Figure 2.1: Schematic representation of the elementary particles of the Standard Model: the twelve fundamental fermions and the five gauge bosons are shown along with its antiparticles and the Higgs boson.

The elementary particles and fundamental interactions are described through the SM Lagrangian,

$$\mathcal{L}_{\text{SM}} = \mathcal{L}_{\text{QCD}} + \mathcal{L}_{\text{EW}} + \mathcal{L}_{\text{Higgs}} + \mathcal{L}_{\text{Yukawa}}, \quad (2-2)$$

where the  $\mathcal{L}_{\text{QCD}}$  term corresponds to the QCD Lagrangian, governing the behavior of quarks and gluons within the strong force framework and it's based on the  $SU(3)_C$  symmetry group (where  $C$  stands for the color charge).  $\mathcal{L}_{\text{EW}}$  describes the electroweak interaction (EW),<sup>5</sup> represented by the  $SU(2)_L \times U(1)_Y$  gauge symmetry, where  $L$  and  $Y$  correspond to left-handed chirality and weak hypercharge, respectively. The Higgs term,  $\mathcal{L}_{\text{Higgs}}$ , introduces the Higgs field, while the Yukawa coupling term,  $\mathcal{L}_{\text{Yukawa}}$ , governs the interaction between fermions and the Higgs field, responsible for giving mass to the fermions. Together, these terms ensure the SM Lagrangian's invariance under transformations of the  $SU(3)_C \times SU(2)_L \times U(1)_Y$  gauge group.

In the context of the SM, it is important to mention the three discrete symmetries in particle physics::

1. Charge conjugation (C): The transformation associated with the exchange of particles and antiparticles, under which all charges (such as electric charge) are reversed;

<sup>5</sup>The electroweak theory is a unification of the QED and the weak interaction theory.

2. Parity transformation (P): Inversion of the spatial coordinates with respect to the origin ( $\vec{r} \rightarrow -\vec{r}$ );
3. Time reversal (T): The transformation of a system corresponding to the inversion of the time coordinate ( $t \rightarrow -t$ ).

The combination of these three symmetries, known as CPT, is conserved according to the CPT theorem as a consequence of Lorentz invariance. While the SM contains CP violation effects, which means that certain processes involving the weak interaction do not conserve CP symmetry, the combination of all three operations (C, P, and T) is still conserved. CP violation in the SM leads to observable differences in the behavior of particles and antiparticles through the weak interactions. The first observation of CP violation occurred in 1964, in the decay of neutral kaons into two pions [25].

While the SM of particle physics provides a successful description of fundamental interactions among elementary particles, there is a general belief that should exist physics beyond the SM. For example, the model doesn't provide a satisfactory explanation for the matter-antimatter asymmetry. Though it predicts certain processes that could potentially generate more matter than antimatter in the early universe, these processes are not sufficient to account for the observed asymmetry [15] [16].

The SM also faces challenges in explaining phenomena like dark matter (DM) and dark energy (DE), which collectively constitute approximately 95% of the universe's energy density. DM, comprising around 25% of their density, interacts gravitationally but does not emit, absorb, or reflect electromagnetic radiation, making it invisible to light and detectable only through its gravitational effects. DE, constituting the remaining 70%, is thought to be responsible for the observed accelerated expansion of the universe, yet its nature remains unclear [12] [13].

Additionally, the SM does not account for neutrino oscillations [14]. These oscillations imply that neutrinos possess mass, a concept that needs to be integrated into the SM Lagrangian. Furthermore, there are some theoretical problems in the SM. The hierarchy of quark and lepton masses is not explained, neither why there are three generations of fermions. Also, the strong CP problem, which concerns the absence of any detectable violation of CP symmetry in strong interactions, remains unresolved.

These unresolved questions suggest the necessity for theories that go beyond the SM, such as Grand Unified Theories (GUTs), Supersymmetry, String Theory and many others.

## 2.2

### The Strong CP problem and axion-like particles (ALPs)

The QCD Lagrangian, denoted by the  $\mathcal{L}_{\text{QCD}}$  term in equation (2-2) and including just one quark, with mass  $m$ , for simplicity, is

$$\mathcal{L}_{\text{QCD}} = -\frac{1}{4}G_{\mu\nu}^a G^{a\mu\nu} + \bar{\psi}^j (i\mathcal{D}_j^k - m\delta_j^k)\psi_k, \quad (2-3)$$

where the first term describes the kinetic energy of gluons and the second term accounts for the interaction between quarks and gluons.  $G_{\mu\nu}^a$  denotes the gluon field strength tensor,  $a$  indexes the eight existing gluon fields,  $\bar{\psi}^j$  and  $\psi_k$  are the quark spinor fields and their conjugates, where the indices  $j$  and  $k$  label the quark flavors; finally,  $i\mathcal{D}_j^k$  is the covariant derivative acting on the quark fields.

Additionally,  $\mathcal{L}_{\text{QCD}}$  allows for an extra term, known as the  $\theta$ -term,<sup>6</sup> expressed as

$$\mathcal{L}_\theta = \theta \frac{g_s^2}{32\pi^2} \tilde{G}_{\mu\nu}^a G^{a\mu\nu}, \quad (2-4)$$

where  $\theta$  is an arbitrary coefficient,  $g_s$  represents the strong coupling constant, which quantifies the strength of the strong interactions in QCD, and  $\tilde{G}_{\mu\nu}^a$  is the dual field strength tensor.

The inclusion of the  $\theta$ -term introduces a violation of CP symmetry into the QCD Lagrangian. From the transformation properties of the gluon field strength tensor ( $G_{\mu\nu}^a$ ) under C, P and T it is seen that the term in equation 2-4 violates both P and T symmetries, and thus CP [27].

The actual physical parameter that measures the strength of CP violating effects in QCD is  $\bar{\theta}$ , defined as

$$\bar{\theta} = \theta + \arg \det[\mathbf{G}^{(U)} \mathbf{G}^{(D)}], \quad (2-5)$$

where  $\mathbf{G}^{(U,D)}$  are complex matrices related to the masses of the up-type and down-type quarks, respectively. These matrices originate from the Yukawa interactions in the SM. To keep the discussion concise, the intricate details of these interactions will not be explored here, but can be found, for example, in ref [27, 28].

The most stringent constraint on the  $\theta$ -term comes from its contribution to the neutron's electric dipole moment,  $d_E(n)$ , which violates P and T symmetries. In 1979, Crewther *et al.* [29] evaluated  $d_E(n)$  using chiral perturbation theory and obtained

$$d_E(n) = (3.6 \times 10^{-16} \bar{\theta}) \text{ e cm}. \quad (2-6)$$

---

<sup>6</sup>This term was first introduced by 't Hooft to address a problem in the QCD, the  $U(1)_A$  problem, more details in [26], [17].

Using the experimental limit [30] of  $d_E(n) < 1.1 \times 10^{-25}$  e cm, one thus finds

$$\bar{\theta} < 3 \times 10^{-10}. \quad (2-7)$$

This experimental observation indicates that CP violation in the strong interaction is extremely small. The SM does not provide a natural explanation for why the  $\bar{\theta}$  parameter is so close to zero, thus leaving what we call *the strong CP problem* unresolved [28].

As a solution to this problem beyond the SM, Roberto Peccei and Helen Quinn proposed in 1977 the introduction of an additional global chiral symmetry, known as  $U(1)_{\text{PQ}}$  symmetry [19]. Under this symmetry the parameter  $\bar{\theta}$  becomes a dynamical variable, which in some conditions relaxes spontaneously to zero, effectively solving the strong CP problem.<sup>7</sup> Shortly after Peccei-Quinn proposal, Weinberg [31] and Wilczek [32] pointed out that since  $U(1)_{\text{PQ}}$  is a global continuous symmetry spontaneously broken by the vacuum, it would lead to the existence of a Goldstone boson, named the *axion* [28].

The axion is predicted to be a neutral pseudoscalar boson with a small mass relative to the spontaneous breaking scale ( $f_a$ ), and it exhibits a well-defined relationship between its mass ( $m_a$ ) and its coupling constant ( $g_a$ ) to SM particles:  $g_a \propto m_a$ . Therefore, in any plot of mass versus coupling strength, axion models would populate a relatively narrow band.

The axion solution to the strong CP problem proposed by Peccei-Quinn is often referred to as the *QCD axion* or the *original axion*, and it is part of a more generic class of models, the axion-like particles (ALPs), which may arise from the breaking of other global symmetries, rather than the  $U(1)_{\text{PQ}}$ .

ALPs are hypothetical spin-0 bosons, similar to the QCD axion but with potentially distinct properties. They can span a much wider range of masses, from as low as  $10^{-22}$  eV up to several GeV, depending on the model, and may couple to photons, fermions, or gluons. Some models also propose ALPs to explain phenomena unrelated to the strong CP problem. For instance:

- light pseudoscalar particles are suggested as candidates for cold DM [33] or as mediators in dark sectors [34];
- generic (pseudo)Goldstone bosons can emerge from the spontaneous breaking of a new  $U(1)$  global symmetry at some high energy scale. Examples include the *familon* (associated with flavor-chiral  $U(1)$  horizontal symmetry) [35], the *R-axion* (linked to broken R-symmetry in SUSY) [36], pseudoscalar states in Higgs compositeness models (from the broken  $U(1)$  symmetry acting on all underlying fermions of the the-

---

<sup>7</sup>Further details on how this mechanism operates can be found in [18], [19],

ory) [37], and pseudoscalar states in models of Higgs compositeness or cosmic inflation [38];

- pseudoscalar bosons may arise in extended Higgs sectors [39], in phenomenological realizations of string theory [40], or models addressing issues like lepton dipole moments (thereby solving the  $(g - 2)_\mu$  problem) [41] or the electroweak hierarchy problem.

Unlike the original axion, ALPs do not have a predictive dependence between coupling and mass, allowing for a more flexible relation between these two parameters. Consequently, ALPs can populate the entire mass vs. coupling plane, providing a broader range of possibilities for their characteristics and enabling researchers to explore various regions of the parameter space in the search for ALPs.

## 2.3

### Searching for ALPs

There are many different sources and methods for which ALPs could be produced and detected. They can be searched across a broad mass spectrum and may couple to different SM particles. For each mass range and coupling possibility, different techniques and approaches can be employed.

ALPs could be emitted by the Sun, the so-called *solar axions*, primarily via Primakoff effect [20],  $\gamma\gamma^{(*)} \rightarrow a \rightarrow \gamma\gamma^{(*)}$ <sup>8</sup> ( $a$  denotes the ALP), where in the presence of the strong electromagnetic field as in the Sun's core, photons would interact with other photons, leading to the production of axions. Through the same process, these axions could be converted back into detectable photons (typically X-rays) utilizing helioscope experiments, such as the Tokyo Axion Helioscope (SUMICO) [42] and the CERN Axion Solar Telescope (CAST) [43]. Another natural source of axions would be the DM present in our universe. If DM is in fact composed in its majority of ALPs, then our galactic halo would be the most productive source of these particles, and they could be detected using haloscope experiments. These experiments use highly sensitive devices designed to identify the faint signals associated with axions in the surrounding environment, such as the Axion Dark Matter eXperiment (ADMX) [44].

Different from natural sources, we are interested in ALPs that could be generated and detected in laboratory, more specifically, in collider experiments. Depending on the energy of the collision and the particles involved, ALPs with different masses and coupling structures can be produced at colliders and decay into photons, charged leptons, light hadrons or jets, which can then be detected.

---

<sup>8</sup>In this context,  $\gamma^{(*)}$  denotes virtual photons involved in the interaction.

Colliders have primarily focused their searches for ALPs on processes involving initial and/or final states containing photons, i.e. on axionic-photon coupling. This focus arises because the coupling between ALPs and photons is one of the most theoretically motivated interactions and is often the most experimentally accessible. The interaction of ALPs with photons is typically described by a Lagrangian of the form:

$$\mathcal{L} = \frac{1}{2}\partial^\mu a\partial_\mu a - \frac{1}{2}m_a^2 a^2 - \frac{1}{4}g_{a\gamma}aF^{\mu\nu}\tilde{F}_{\mu\nu}, \quad (2-8)$$

where  $a$  is the ALP field,  $m_a$  is the ALP mass,  $F^{\mu\nu}$  ( $\tilde{F}_{\mu\nu}$ ) is the photon field strength (dual) tensor and  $g_{a\gamma}$  is the coupling constant to photons, which is linked to the high-energy scale<sup>9</sup>  $\Lambda$  associated with the broken symmetry in the ultraviolet by the relation:  $g_{a\gamma} \propto \frac{1}{\Lambda}$ . Thereby, the entire ALP phenomenology can be characterized within the  $(m_a, g_{a\gamma})$  parameter space.

### 2.3.1

#### Ultrapерipheral collisions (UPC)

ALPs that directly couple to photons may be produced in a modification of the light-by-light (LbL) scattering channel,  $\gamma\gamma \rightarrow \gamma\gamma$ . LbL scattering is a process in the SM that occurs at the lowest order in QED through virtual one-loop box diagrams involving charged fermions and  $W^\pm$  bosons [9]. The probability of two photons interacting in this manner is quite low, requiring a large flux of photons for the possibility of a single scattering event to occur.

Therefore, LbL scattering is more likely to occur as a subprocess in ultraperipheral collisions (UPC), where the impact parameter is larger than twice the radius of the nuclei (as shown in Fig.2.2), making the two ions interact via their cloud of virtual photons. The electromagnetic (EM) fields generated by the colliding nuclei can be treated as a beam of quasi-real photons of virtuality  $Q^2 < \frac{1}{R^2}$ , where  $R$  is the radius of the nuclear charge distribution. Additionally, the intensity of these EM fields, and consequently the number of photons in the cloud surrounding the nucleus, scales with  $Z_1^2 Z_2^2$  (where  $Z_i$  are the atomic numbers of the incident particles) [1]. Thus, these interactions are significantly favored in ultraperipheral heavy ions collisions (UPHIC).

---

<sup>9</sup>This scale is approximately the same as the  $f_a$  energy scale at which the spontaneous breaking of the  $U(1)PQ$  symmetry occurs

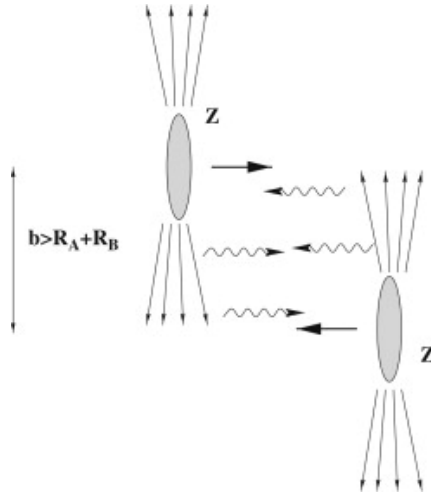


Figure 2.2: Schematic diagram of an UPC of two ions, where  $Z$  is the atomic number and the impact parameter,  $b$ , is larger than the sum of the two radii,  $R_A + R_B$  [1].

For lead (Pb) nuclei with  $R \approx 7$  fm, the quasi-real photon beams have virtualities  $Q^2 < 10^{-3}$  GeV and the LbL scattering cross sections in PbPb collisions are enhanced by a factor of  $Z^4 \approx 5 \times 10^7$  compared to similar proton-proton or electron-positron interactions. The final state signature of interest is the exclusive production of two photons,  $\text{Pb} + \text{Pb}(\gamma\gamma) \rightarrow a \rightarrow \text{Pb}^{(*)} + \text{Pb}^{(*)} \gamma\gamma$ , where the outgoing Pb ions (with a potential EM excitation denoted by the  $(*)$ ) survive the interaction as shown in Fig.2.3, a.

One of the primary advantages of conducting ALPs searches in UPHIC is the cleanliness of the resulting final state, which entails minimal background contamination. This final state consists of the diphoton system, two intact nuclei and two rapidity gaps, which represent empty regions in pseudo-rapidity, effectively separating the intact, very forward nuclei from the  $\gamma\gamma$  system [21].

However, to effectively probe the presence of ALPs in the  $\gamma\gamma \rightarrow a \rightarrow \gamma\gamma$  channel, it is crucial to distinguish these associated events from those arising in the LbL scattering, in which the diphoton final state is created by the elementary elastic  $\gamma\gamma \rightarrow \gamma\gamma$  subprocess (Fig.2.3, b), and from the QED production of an exclusive electro-positron pair (dielectron production), where both the electron and positron can be misidentified as photons (Fig.2.3, c).

By analyzing the measured diphoton invariant mass distribution and carefully identifying potential backgrounds, if no signal is observed, new exclusion limits can be set for ALPs production, specifically in the  $(m_a, g_{a\gamma})$  parameter space. The search for ALPs in these type of collisions were proposed in [45].

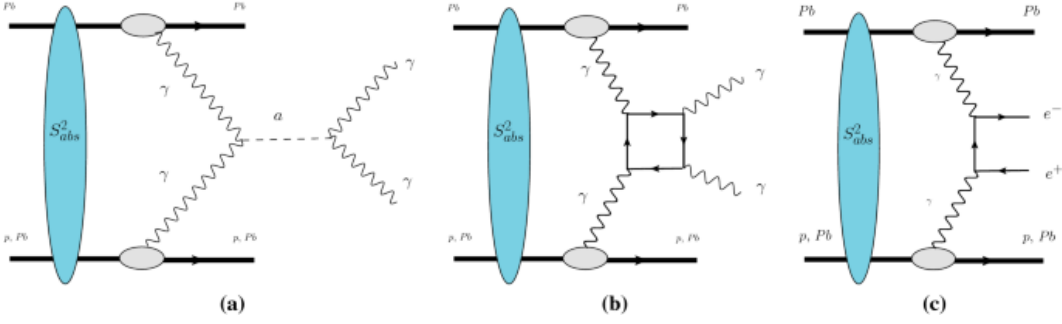


Figure 2.3: Representation of diphoton production in PbPb or pPb collisions by (a) the  $\gamma\gamma \rightarrow a \rightarrow \gamma\gamma$  subprocess and (b) Light-by-Light scattering. (c) The dielectron production, which is an important background when the electrons are misidentified as photons.  $S_{abs}^2$  is the absorptive factor, and it depends on the impact parameter,  $b$ , of the PbPb collision [2].

### 2.3.2

#### Current status of ALPs searches

This section contains a short overview of the current status of axion and ALPs searches in terms of the photon coupling scenario. This review is a summary mostly based on ref [3].

The  $(g_{a\gamma}, m_a)$  plane is where limits are set for the existence of ALPs characterized by a specific coupling constant ( $g_{a\gamma}$ ) and mass ( $m_a$ ). The shaded areas in the parameter space represent excluded regions, where certain experimental data have ruled out the existence of ALPs with the  $(g_{a\gamma}, m_a)$  combination present in that area.

The current limits in ALP mass ( $m_a$ ) and in ALP- $\gamma$  coupling ( $g_{a\gamma}$ ) are shown in Fig.2.4. For  $m_a < 10^{-8}$  GeV, the constraints come from experiments such as light-shining-through-a-wall (LSW) and the ones based on helioscopes methods (CAST and SUMICO), indicated by the colors purple and blue. In the middle of the plot, the limits are imposed by astrophysical studies that have been established by the energy dissipation of stars due to ALPs emissions, determined through observations such as the ratio of red giants to younger stars on the horizontal branch (HB, in light-green area), the measurement of the length of the neutrino burst from supernova SN1987a (yellow) [46], and the absence of photon bursts from supernovae resulting from the decay of generated ALPs (dark-green). The grey region, including the triangle below the beam-dump limits, represents the combination of the cosmological constraints over  $m_a \approx 1\text{keV}$  to 10 GeV [47]. In the region of fixed-target proton and electron experiments (Beam dump, in orange), ALPs are searched in final states with single photons or diphotons emitted in the forward direction [48].

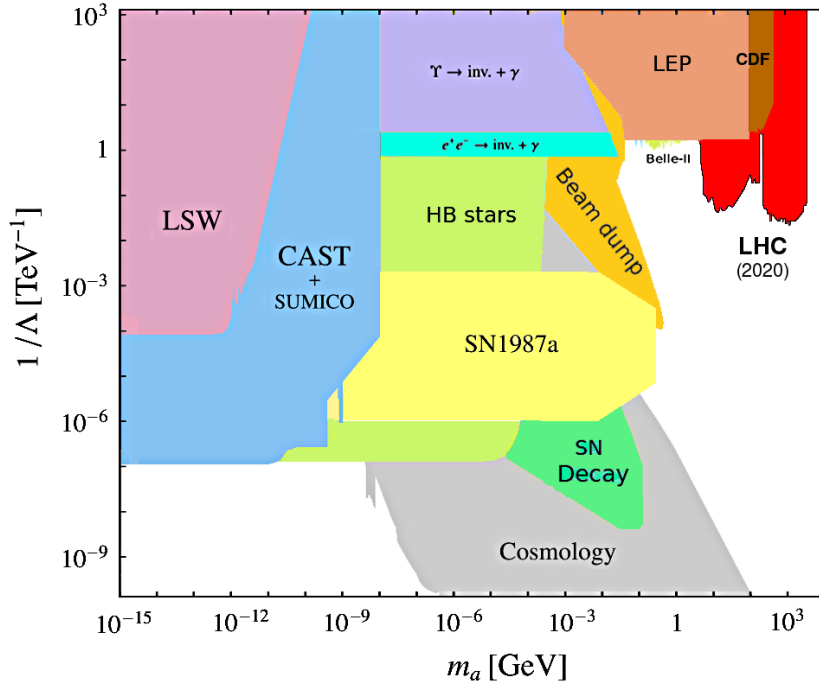


Figure 2.4: Current limits on the ALP-photon coupling vs. ALP mass from cosmological, astrophysical, and accelerator searches [3].

Apart from the weakly coupled ones (with  $g_{a\gamma} < 10^{-6} \text{ TeV}^{-1}$ ), which have already been ruled out by cosmological observations, ALPs with masses above 1 GeV can only be accessed via collider experiments. The top-right area of Fig.2.4 can be zoomed-in as shown in Fig.2.5. Searches conducted at  $e^-e^+$  colliders focus on various final state configurations. These include mono-photon final states, observed through decays such as  $\Upsilon \rightarrow \gamma a$  (light-purple area of Fig.2.5) and interactions like  $e^-e^+ \rightarrow \gamma a$  (light-blue) at facilities like CLEO and BaBar [49]. Additionally, diphoton and triphoton final states, arising from processes like  $e^-e^+ \rightarrow 2\gamma, 3\gamma$ , are investigated for masses ranging from 50 MeV to 8 GeV and 20 to 100 GeV, respectively, conducted at LEP-I and II [50] (dark-orange). Similar searches have been undertaken at Belle-II [51] (light-green), PrimEx [52] and CDF [53] (brown).

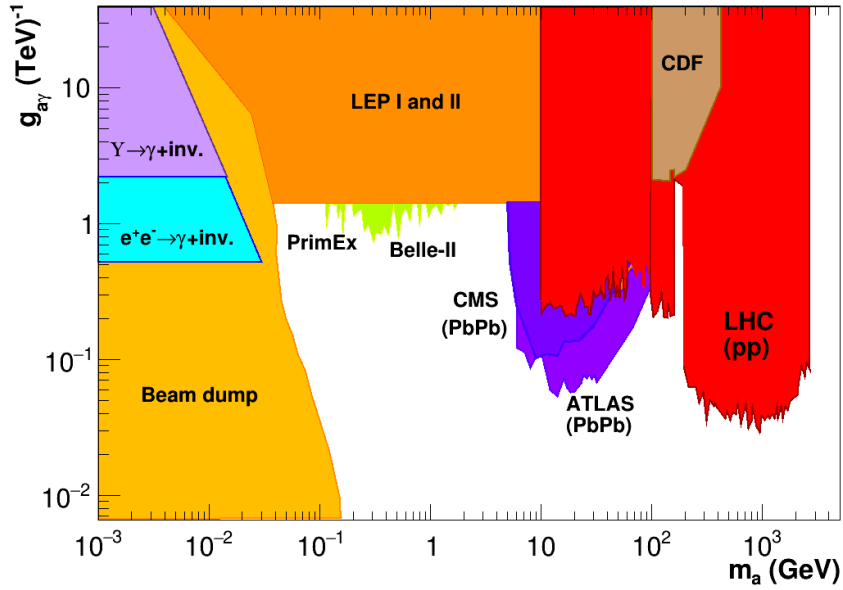


Figure 2.5: Detailed bounds in the  $(m_a, g_{a\gamma})$  plane from all existing accelerator and collider ALP searches for masses  $m_a \approx 1 \text{ MeV} - 3 \text{ TeV}$  [3].

Searches at CERN's LHC (red and dark-purple areas in Fig.2.5) predominantly concentrate on final states involving photons and, occasionally,  $Z$  and Higgs bosons. Significant searches have been set for ALPs with masses  $> 5 \text{ GeV}$  in 2-, 3-, 4-photon final states configurations. These searches explore both exclusive and inclusive  $\gamma\gamma$  resonances, along with the investigation of exotic decays involving  $Z$  or Higgs bosons. Diagrams illustrating these processes are shown in Fig.2.6. The exclusion limits labeled "LHC( $pp$ )" and "CMS(PbPb) and ATLAS(PbPb)" in Fig.2.5 are mostly based on  $pp$  collision and UPHIC (with lead) data from ATLAS [9] and CMS Collaborations [8]. Recent results from ATLAS, with searches in  $H \rightarrow aa \rightarrow 4\gamma$ , can be found in [54].

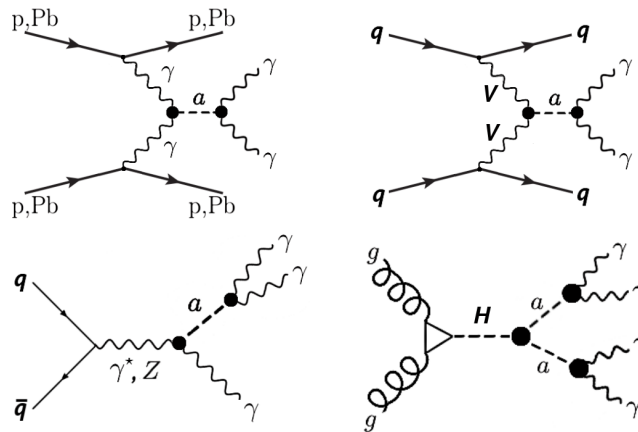


Figure 2.6: Representative diagrams of ALPs searches at the LHC via exclusive diphotons (topleft), diphotons from vector-boson-fusion (with  $V = \gamma, Z$ , top right), exotic triphoton  $Z$ -boson decays (bottom left), and exotic 4-photon Higgs-boson decays (bottom right) [3].

In the exploratory study conducted in [21], the authors have demonstrated that a forward detector, such as the LHCb detector, is well-suited for investigating ALPs with low masses ( $m_a < 10$  GeV), a mass range that is challenging for ATLAS and CMS detectors due to limitations in reconstructing photons. The analysis focused on PbPb collisions and examined ALP production under four different combinations of mass and coupling. The study was further complemented in [2], where the analysis was expanded to include a broader range of mass and coupling combinations, and also considered ultraperipheral collisions of  $p$ -Pb. To assess the LHCb detector's potential for detecting ALPs in these scenarios, the authors derived its expected sensitivity, considering different luminosities and selection criteria, as shown in (Fig.2.7). Overall, this study highlighted the potential for LHCb to contribute to ALP searches involving photon coupling and production in UPC, potentially leading to new exclusion regions in the  $(g_{a\gamma}, m_a)$  parameter space.

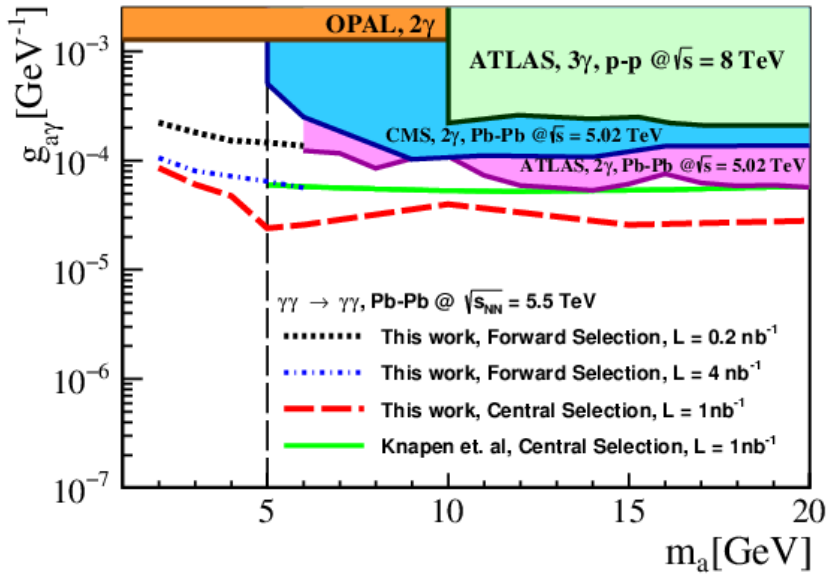


Figure 2.7: Expected sensitivity to the ALP production in PbPb ultraperipheral collision. "This work" refers to [2].

## 3

### The LHC and the LHCb experiment

This chapter describes the experimental setup used to produce the data analyzed in this dissertation. A description of the Large Hadron Collider (LHC) and the LHCb experiment is given, with special emphasis on the most relevant subsystems used for photon detection. The content of this chapter is primarily based on the detailed descriptions found in references [55] and [5].

#### 3.1

##### The LHC

The Large Hadron Collider (LHC) [55] is a circular collider designed for proton-proton ( $pp$ ) and heavy ion (such as lead) collisions. It was built between 1998 and 2008 by CERN with approximately 27 kilometers of circumference and situated around 100 meters underground, at the French-Swiss border near Geneva (Fig.3.1).

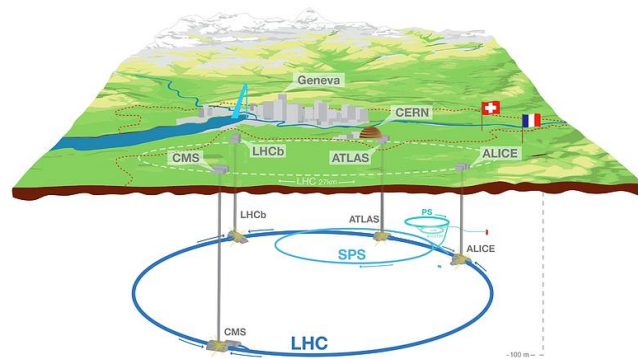


Figure 3.1: The LHC underneath the French-Swiss border, near Geneva.

Before entering the LHC for acceleration to energies up to 7 TeV, the proton beams undergo a series of acceleration stages in lower-energy particle accelerators. During Run 2, these accelerators include the *Linear Accelerator 2* (LINAC2), the *Proton Synchrotron Booster* (PSB), the *Proton Synchrotron* (PS) and the *Super Proton Synchrotron* (SPS), as one can see in Fig.3.2. Protons are initially obtained from hydrogen atoms coming from a hydrogen bottle, with electrons stripped off using an electric field. Afterwards, they are accelerated by LINAC2, followed by sequential acceleration stages in PSB, PS and SPS, gradually increasing their energy. Finally, protons exiting the

SPS are injected into the LHC at energy level of 450 GeV. For heavy ions, the acceleration process begins with the *Linear Accelerator 3* (LINAC3), from where ions are directly injected into the PS, after the PSB stage.

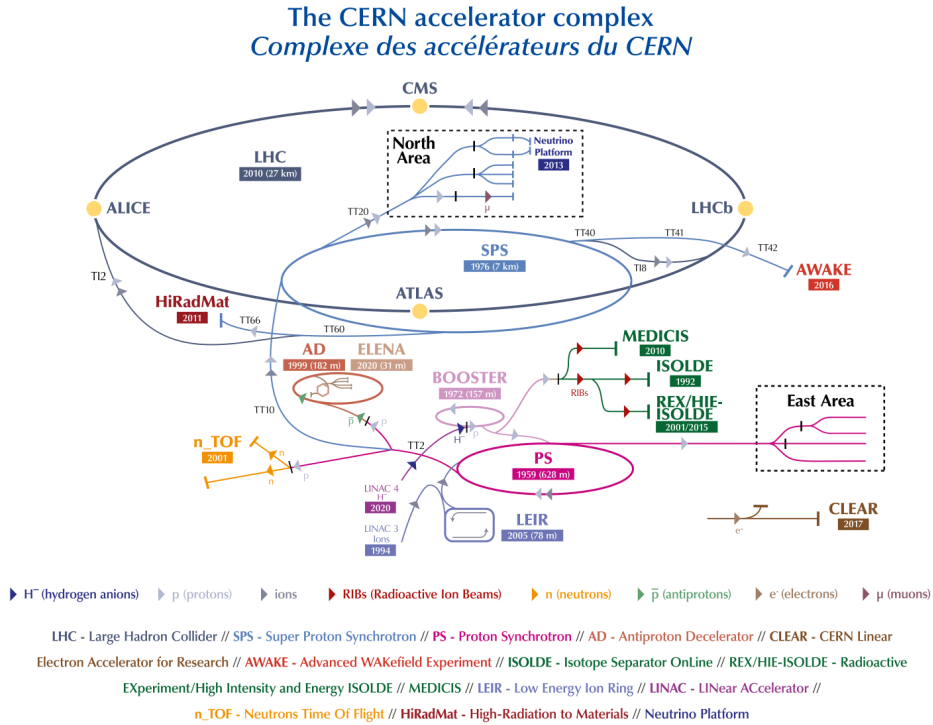


Figure 3.2: CERN's accelerator complex.

The beams accelerated by the LHC are made to collide at four different interaction points (IP) around the accelerator ring. These points are surrounded by the four primary experiments at the LHC: ATLAS, ALICE, CMS and LHCb. These experiments can be categorised into two classes: the general-purpose detectors (GDPs) and specialized detectors dedicated to specific physics objectives. ATLAS [22] and CMS [23] experiments, situated at IP1 and IP5, respectively, are the GDPs. They are nearly hermetic detectors that are specialised in high- $p_T$  physics, in measuring the properties of the top quark and the Higgs boson as well as in direct searches for physics beyond the SM. The two large and more specialised LHC experiments are the ALICE [56] and LHCb [5] experiments. The ALICE experiment, located at IP2, studies the properties of the quark-gluon plasma in heavy ion collisions. The LHCb experiment, located at IP8, is designed for precision measurements in the field of heavy-flavour physics. Its main purpose is the study of CP violation and the indirect search for physics beyond the SM in decays of charm and beauty hadrons. Over time, LHCb's physics program has evolved into a more general-purpose experiment making significant contributions to other fields such as

hadron spectroscopy, heavy ion and electroweak physics. Further details about the LHCb experiment will be provided in the following section.

### 3.2 The LHCb detector during Run 2

The LHCb detector is a single-arm forward spectrometer with a angular acceptance of 10 to 300 mrad in the horizontal plane ( $zx$ ) and 10 to 250 mrad in the vertical plane ( $yz$ ) of the detector, which is equivalent to a pseudorapidity of  $2 < \eta < 5$ . This angular range is motivated by the fact that at high energies both quarks from the  $b\bar{b}$  (or  $c\bar{c}$ ) pairs are predominantly produced at small angles with respect to the beam pipe.

The LHCb consists of a tracking system, two ring imaging Cherenkov detectors (RICH1 and RICH2), a calorimeter and a muon systems (M1-M5). The tracking system, which is responsible for the momentum reconstruction of charged particles, is composed of the vertex locator (VELO), the tracker turicensis (TT stations), a magnet and three tracking stations: T1, T2, T3. The calorimeter system, responsible for the energy reconstruction, is composed of a Scintillator Pad Detector (SPD), a PreShower (PS), an Electromagnetic CALorimeter (ECAL) and a Hadronic CALorimeter (HCAL). The calorimeter system along with the RICH detectors and the muon chambers are part of the LHCb particle identification (PID) system. The Fig.3.3 show a view of the detector.

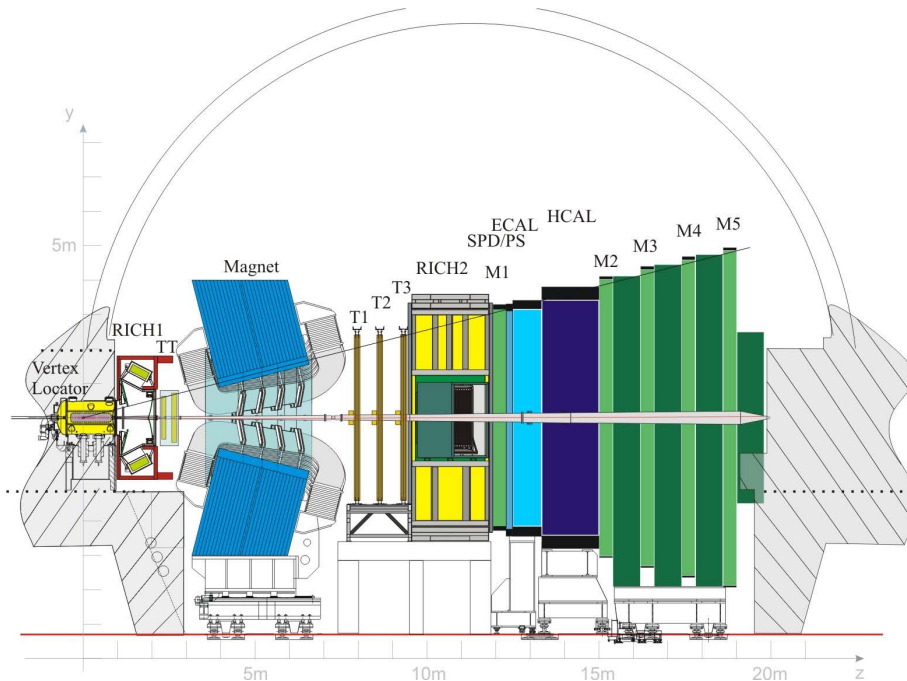


Figure 3.3: Schematic overview of the LHCb detector layout during the Run 1 and Run 2 data takings. Taken from [4].

During the period from 2013 to 2014, a new subdetector, the HeRSChel (High Rapidity Shower Counters for LHCb), was installed for Run 2 of the LHC, which began in 2015, with the aim of enhancing LHCb's capabilities in diffractive physics, particularly by improving background suppression in analyses of Central Exclusive Production (CEP) and Ultraperipheral Heavy-Ion Collisions (UPHIC). Detailed information about this detector can be found in ref [7].

### 3.2.1

#### Tracking system

The vertex locator (VELO) is the first detector seen by the particles and the closest one to the interaction point (IP8). Its purpose is to reconstruct the primary and secondary vertices of  $pp$  collisions and of the particles flying both in the forward and the backward directions. The straight trajectories of the charged particles produced are built from hits recorded in the VELO and are furthermore matched to the hits seen in the following tracking chambers. Moreover, two specific sensor layers of the VELO located in the backward region are used for the first level trigger in order to veto pile-up events.

The Tracker Turicensis (TT) are located between the RICH1 and the dipole magnet. They have mainly three purposes. First, they permit to have intermediate hits between the VELO and the tracking stations T1-T3 located on the other side of the magnet, which improves the momentum resolution of long tracks and reduce the amount of fake tracks, falsely reconstructed by the pattern recognition of the tracking algorithms. More specifically, the TT enables the reconstruction of tracks of low momentum particles that are swept by the magnetic field, and do not reach the T1-T3 stations. Finally, they give a significant additional information to reconstruct the neutral long-lived particles such as  $K_s^0$ , that decay outside the VELO volume.

The dipole magnet produces a field  $\mathbf{B}$  in the  $y$ -direction that imposes a curvature to the charged particles in the  $xz$  horizontal plane, and consequently permits deduce their sign and momentum. The larger and better known the magnetic field, the better the momentum resolution. The field strength  $B_y$  as a function of the  $z$ -position is shown in Fig.3.4. The magnet can be operated in two polarities *MagUp* and *MagDown* by inverting the direction of  $B_y$ , which is done to reduce systematic uncertainties in the measurements.

The tracking chambers T1, T2 and T3 complete the track and momentum reconstruction after the magnet bending. The tracking algorithms are written to connect the hits from the sensors in the tracking system and reconstruct the trajectories given the known and imposed magnetic field. There are five

different track types that can be reconstructed in the LHCb, differing on which sub-detector contain information about it. These types are listed below and illustrated in Fig.3.4.

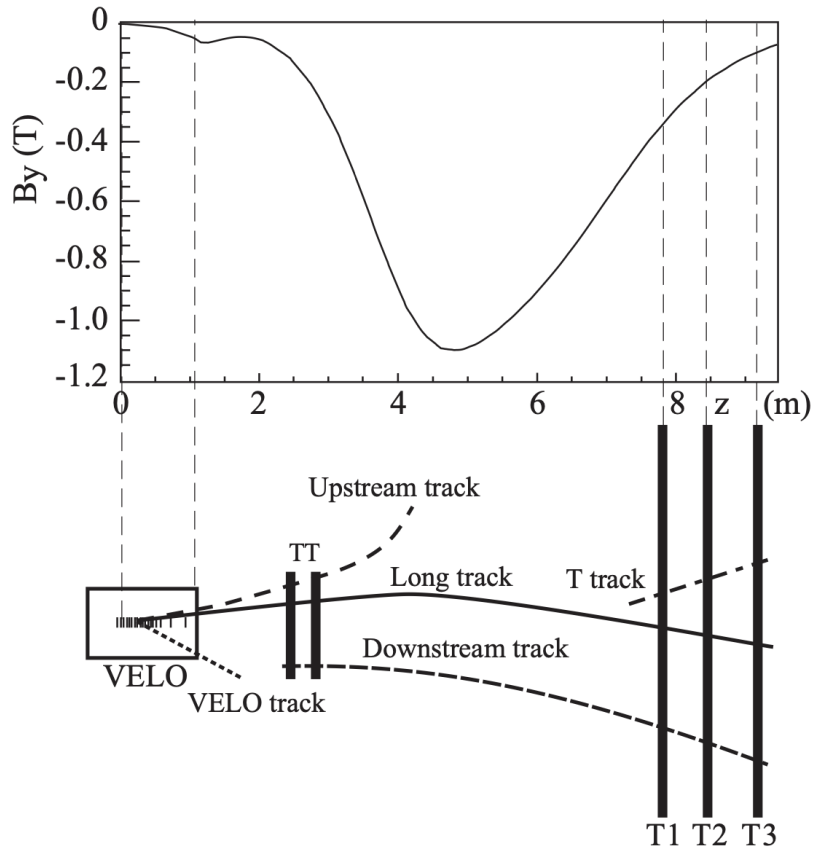


Figure 3.4: Strength of the magnet field component  $B_y$  as a function of the  $z$  coordinate in the different tracking detectors of LHCb and overview of the track types reconstructed in the LHCb. Taken from [5]

- Long tracks: tracks that traverse the full tracking system leaving hits in the VELO, the T1-T3 stations, and possibly in TT as well. Therefore, long tracks have the most precise momentum determination;
- Downstream tracks: tracks with hits in the TT and T1-T3 stations. These tracks correspond to particles produced by decays that happened outside of VELO;
- Upstream tracks: tracks that leave hits in the VELO and the TT, and are bent out of the detector acceptance by the magnetic field before reaching the T1-T3 stations. They are mostly low-momentum tracks;
- T tracks: tracks that only leave hits in the T1-T3 stations. They are typically produced in secondary interactions and are useful for the global pattern recognition in RICH2;

- VELO tracks: tracks with hits only in the VELO. They are typically large angle or backward tracks, and useful for the reconstruction of primary vertices.

### 3.2.2

#### Particle identification

The Ring Imaging Cherenkov detectors located on both sides of the magnet, called RICH1 and RICH2, are responsible for separate the various species of hadrons. The RICH detectors permit to identify specific hadronic decays with high efficiency and low contamination. The LHCb has two of them because they operate in well-defined momentum range, so each of them is specialised in two overlapping momentum ranges. RICH1 looks at the full LHCb acceptance in a momentum range from low values up to 60 GeV, while RICH2 identifies particles whose momentum exceeds 15 GeV up to 100 GeV and consequently whose pseudorapidity is rather large. From the determined radius of the Cherenkov ring reconstructed, the medium index and the momentum of the tracks (obtained from the tracking system), the mass of the particle can be measured and thus its type.

The muon stations are supposed to detect what has not yet been absorbed by the other sub-detectors, i.e the muons that have a large penetration power. It is composed of five stations, M1-M5, positioned along the beam line. The first station, M1, is located immediately after RICH2 and just before the calorimeter system (next section), while the M2-M5 are located right after it and at the end of the LHCb detector. M1 is built from Gaseous Electron Multiplier (GEM) detectors because of the occupancy and radiations in the corresponding region while M2, 3, 4 and 5 are equipped with multi-wire proportional chambers (MWPC).

#### 3.2.2.1

##### The calorimeter system

Because this is where the photons are identified, we dedicated a separated section for the calorimeter system, positioned between the first and the second muon stations. Its layout is shown in Fig.3.5. This system is responsible for the identification of hadrons, electrons and photons and the measurement of their energies and directions. As mentioned before, this system is composed of four sub-detectors: the Scintillator Pad Detector (SPD), the PreShower (PS), the Electromagnetic Calorimeter (ECAL) and the Hadronic Calorimeter (HCAL).

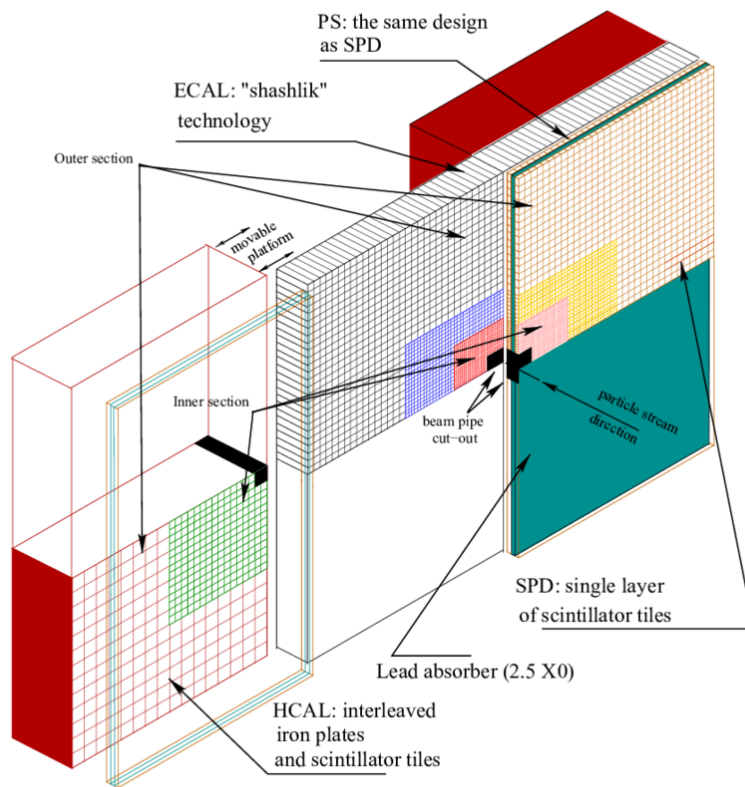


Figure 3.5: Layout of the calorimeter system. Taken from [4].

All four sub-detectors use scintillating material to detect traversing particles. The wavelength of the scintillation light is shifted by a wavelength shifter before it is brought to the Photo Multipliers (PMTs) in case of the ECAL and HCAL or to the Multi-Anode Photo Multipliers (MAPMTs) of the SPD and PS.

The SPD and PS are panels of scintillator pads (cells), with 6016 cells each. They are interleaved with a lead panel which has the purpose of inducing an electronic shower when crossed by an electron or a photon. A signal in the SPD marks the presence of a charged particle, while a signal in the PS indicates that an electronic shower has been created by the lead wall. Coincident signals in the SPD and PS indicate an electron, while a PS-only signal indicates a photon. Furthermore, the number of signals in the SPD gives a quick estimate of the number of charged particles crossing the detector, also known as charged multiplicity.

The ECAL is also composed of 6016 cells. It is divided in three regions, inner, middle and outer, with varying granularity, as illustrated in Fig.3.6. The closer a section is to the beam, the smaller the employed cells are. Furthermore, the cell size is such that the SPD-PS-ECAL system is projective, as seen

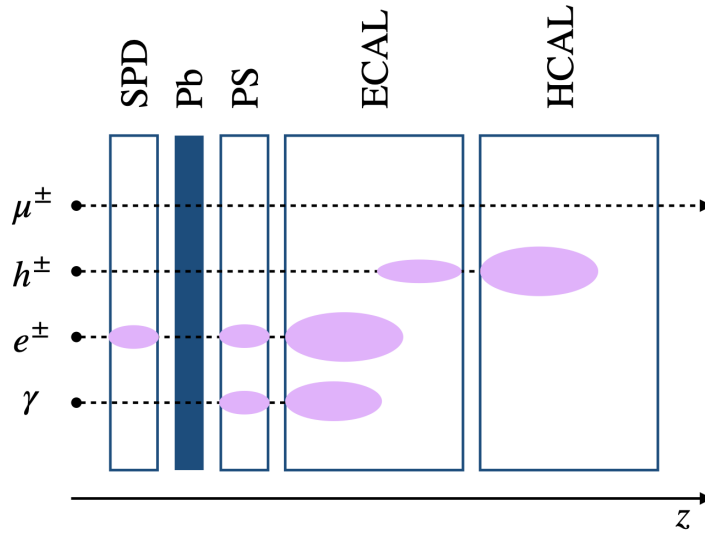


Figure 3.7: Sketch of the expected energy deposition in the various subdetectors of the calorimeter system by different species of particles. Taken from [6]

from the interaction point. The ECAL cells have a shashlik structure, with alternating scintillator and lead layers. The HCAL is composed of 1488 cells, which are composed of alternating scintillator and iron layers. The HCAL is divided in two sections, as illustrated in Fig.3.6. Again, the inner section has higher granularity. ECAL and HCAL determine the electromagnetic or hadronic nature of the particles reaching them.

Fig.3.7 shows the expected energy deposition of muons, hadrons, electrons and photons in the calorimeter system.

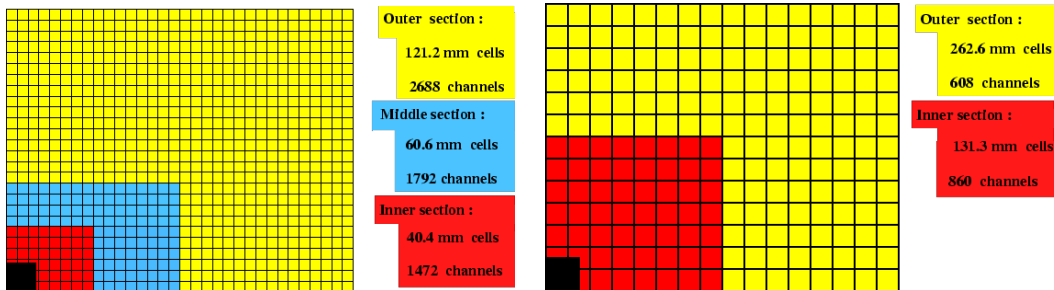


Figure 3.6: Calorimeter cells segmentation of the SPD, PS, and ECAL (left), and the HCAL (right). Taken from [4].

The identification capabilities and disentangling of electrons, photons and hadrons by the calorimeter system comes from crossing information from SPD, PS, ECAL and HCAL. The reconstruction and identification of electrons and photons in the calorimeter is performed by clustering algorithms that group together hits from neighbouring cells. Clusters that cannot be matched to tracks extrapolated to the ECAL or hits in the SPD are likely to come from photons, whereas clusters that can be matched are interpreted as electrons.

The ratio of deposited energy in the ECAL over the momentum of the matched track, taken from the tracking system, gives a powerful discrimination between electrons that deposit most of their energy in the ECAL and hadrons that only leave small amounts in the ECAL and most of their energy in the HCAL. Electrons that are bent in the magnetic field can also lose energy by radiating bremsstrahlung photons that create clusters in the ECAL themselves. A dedicated bremsstrahlung recovery algorithm is responsible for attaching these clusters to reconstructed electron tracks to correct their measured momentum.

The SPD threshold is set so that only charged particles give a hit. The PS, being located after a lead absorber, measures a sizable energy deposit for electrons and photons. The ECAL fully absorbs the electromagnetic particles (photons and electrons). The HCAL mainly absorbs the hadrons. There is a lead converter, between the SPD and the PS, that allows to initiate the electromagnetic showers so that electrons and photons deposit a sizable amount of energy in the PS.

Charged particles leave in SPD a minimum ionising particle (mip) signal which is detected while photons do not interact. Combining the SPD and PS information with the cluster position reconstruction of the ECAL gives a determination of the nature of the electromagnetic particle interacting with the calorimeter system.

The calorimeter system is also crucial for the Level-0 (L0) hardware trigger. The hit multiplicity in the SPD is used to discard events with large track multiplicity that slow down the reconstruction in following software triggers. The energy in the transverse plane ET provided by ECAL and HCAL is used to trigger on interesting events containing high-ET electron, photon and hadron events. The trigger system is discussed in more detail in the following section.

### 3.2.3

#### Trigger and acquisition

The LHCb employs a trigger system, i.e a filtering system, in order to reduce the amount of data to be permanently stored. The trigger system operates at two levels. The first one is a Level-0 (L0) hardware trigger followed by a high-level software trigger (HLT) with two stages (HLT1 and HLT2). Fig.3.8 shows a schematic overview of the trigger stages as they were operated in Run 2. The  $pp$  bunch crossing rate at LHCb corresponds to 40 MHz. This also includes empty bunches so that the effective collision rate of visible interactions is reduced. In Run 2 it corresponded to about 30 MHz. The amount of event data resulting from colliding proton bunches at 30 MHz is by far too high

to store every event. Moreover, many of the processes studied at LHCb are rare, so that many other events are not of interest. Therefore, the three stages of the trigger system are responsible for filtering out interesting events for the physics studied at LHCb while discarding a large amount of uninteresting events in order to decrease the rate down to 12.5 kHz. A set of trigger selection requirements for a specific process or type of physics is usually referred to as a trigger line in LHCb.

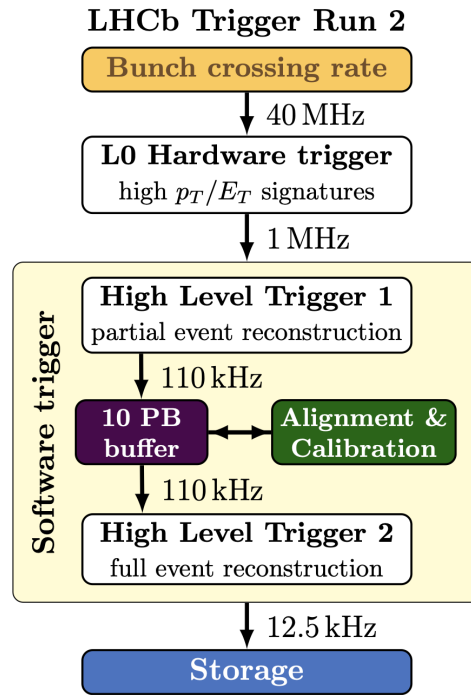


Figure 3.8: Stages of the LHCb trigger system and their event rates during Run 2.

The L0 trigger uses basic information collected from the calorimeter, the muon chambers and the VELO to reduce the rate from 40 MHz to 1 MHz. Due to the large mass of the B meson, its decay products have a high probability to have high transverse momentum or energy. Thus the L0 trigger is a fast hardware trigger aiming at reconstructing the highest transverse energy hadron, electron and photon clusters in the calorimeters as well as the two highest transverse momentum muons in the muon chambers. Hadron, electron and photon candidates are built based on their signature in the calorimeter only. If the energy of the L0Hadron, L0Electron or L0Photon candidates or the momentum of the L0Muon candidates is above a predefined threshold, the corresponding trigger line is fired and the event is kept.

The High Level Trigger (HLT) applies a full event reconstruction, and reduces the rate to a few kHz. The first stage HLT1 only uses part of the full event data. The main purpose of HLT1 is to select beauty or charmed

decays. Thus, using only information from the trackers and the VELO, the HLT1 software performs a partial reconstruction of the tracks. Events are then selected by making some requirements on track quality, momentum and displaced vertices. The rate of events is thus reduced to a few tens of kHz. The events which pass HLT1 then go to HLT2. This second step performs a full reconstruction using the information from all subdetectors. Once the event is fully reconstructed, HLT2 fires when an event matches the requirements of one of the HLT2 lines.

The events which have fired the L0 trigger in the first place and then one or several HLT lines are then saved to disk. However, since these trigger lines are very general, each physics analysis is only interested in some specific decays and thus only uses a small fraction of the data collected at LHCb. To prevent unnecessary disk usage (and costs) the datasets are further split in several streams called stripping lines. Each stripping line corresponds to a loose set of cuts to select events of a given type.

### 3.2.4

#### HeRSChel detector

HeRSChel (High Rapidity Shower Counters for LHCb) [7] is a system of Forward Shower Counters (FSCs) located in the LHC tunnel on both sides of the LHCb interaction point. This detector, consisting of plastic scintillators arranged in five stations (two forward and three backward), was designed to enhance LHCb’s capabilities in diffractive physics, in particular Central Exclusive Production (CEP) and Ultrapерipheral collisions (UPC) analyses.

Each FSC comprises a quadrant of scintillator planes equipped with photomultiplier tubes (PMTs) that are read out synchronously with the LHCb spectrometer’s subdetectors. The planes are situated close to the beam pipe and detect showers induced by very forward particles interacting in the beam pipe or other machine elements. In this manner HeRSChel provides sensitivity to activity at higher rapidities ( $5 \lesssim |\eta| \lesssim 10$ ) than is available from the other sub-detectors of the experiment. This increased acceptance will be valuable in the classification of different production processes in LHC collisions, for example the isolation of CEP and UPC candidates.

As shown schematically in Fig.3.9, the HeRSChel system comprises three stations at negative  $z$ , known as “backward” or “B” stations, and two stations at positive  $z$ , known as “forward” or “F” stations. The active element of each station is a plastic scintillator plane with outer dimensions of 600 mm  $\times$  600 mm, centered around the beam line. The shape and dimensions of the inner opening depend on the local vacuum chamber layout. Stations B0, B1, and F1

have circular holes with radii of 47 mm (B0, B1) and 61 mm (F1), respectively. For stations B2 and F2, the inner opening has a half-width of 115 mm in the horizontal direction (to encompass the two vacuum chambers), and a half-width of 54 mm in the vertical direction.

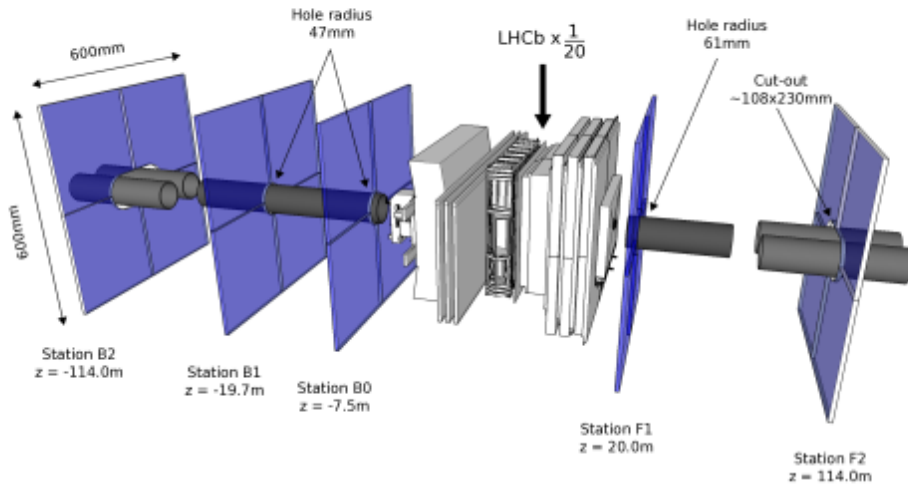


Figure 3.9: Schematic view of the HeRSChE L stations around the LHCb interaction point, where for illustration the HeRSChE L stations have been magnified by a factor of 20 with respect to the rest of the LHCb detector. The  $z$ -axis is not to scale. Image adapted from [7].

### HeRSChE L variable

The variable used in this analysis for HeRSChE L requirement is modeled as  $\ln(\chi^2)$ , and is defined as

$$\ln(\chi^2) = \sum_{i=1}^{20} \left( \frac{ADC - \mu_i}{\sigma_i} \right)^2, \quad (3-1)$$

where  $\mu_i$  and  $\sigma_i$  are the mean and sigma of pedestal of the  $i$ -th HeRSChE L channel, in total 5 stations  $\times$  4 quadrants = 20 channels [57].

## 4

### Analysis of ALP searches at LHCb during Run 2

This chapter presents the strategy and results of our analysis. We begin by introducing key statistical concepts, with a particular focus on the  $CLs$  method for setting upper limits. Then, we outline the key kinematic variables and the selection criteria applied to distinguish signal from background. The chapter concludes with the presentation of the expected exclusion limits, emphasizing the blind nature of current stage of this analysis.

#### 4.1

##### Analysis Strategy

Currently, no evidence of ALP production has been observed at the LHC or any other experiment, and upper limits on ALP coupling constant have been established, as discussed in the last section of Chapter 2. Interpreting the results of searches for new particles and phenomena near the sensitivity limits of an experiment is challenging due to factors like background levels and experimental resolution.

Therefore, the goal of a search is either to exclude the existence of a signal or confirm its presence, while ensuring that the probabilities of falsely excluding a true signal or falsely discovering a non-existent one remain at or below specified levels. To achieve this, various statistical methods are employed to interpret experimental results, each offering a distinct approach to hypothesis testing and the derivation of confidence intervals and upper limits. Common methods include Bayesian approaches and pure frequentist ones [58]. Although these methods are conceptually interconnected, we have chosen to use the  $CLs$  method, also known as the *modified frequentist approach*, for our analysis due to its suitability in handling small statistical samples [59].

Our strategy follows a blind analysis approach, meaning that the final data sample is not inspected until the analysis has been fully validated and reviewed by the LHCb collaboration. This ensures that the selection criteria and statistical methods are applied impartially, without bias from the actual data [60]. Similar to the analyses conducted by ATLAS and CMS [8, 9], we aim to select events with two reconstructed photons and an exclusive topology, considering the main backgrounds to be the dielectron production from QED processes and diphoton production from Light-by-Light (LbL) scattering, as illustrated in Fig. 4.1. The main goal of our analysis is to set upper limits on the ALP coupling constant using the  $CLs$  method. We achieve this by comparing

the expected signal events from Monte Carlo simulations of ALPs with the expected background events from dielectron and LbL simulations.

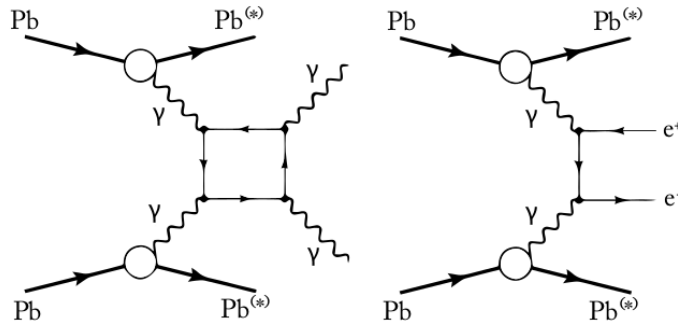


Figure 4.1: Feynman diagrams for possible interactions in ultraperipheral PbPb collisions at the LHCb. Left: diphoton production in a LbL scattering. Right: QED dielectron production. A potential electromagnetic excitation of the outgoing Pb ions is denoted by (\*). Taken from [8].

#### 4.1.1

##### Setting upper limits with the *CLs* method

Before presenting the *CLs* method, we need to define some statistical concepts that will be important for understanding what follows. These definitions are mostly based on Ref. [61].

- *Null Hypothesis* ( $H_0$ ): Also known as the *background-only* hypothesis ( $H_b$ ). It represents the scenario where no discovery is made (i.e., there is no deviation from the SM). The observed results are well described by the SM.
- *Alternative Hypothesis* ( $H_1$ ): Also known as the *signal+background* hypothesis ( $H_{s+b}$ ). This hypothesis is favored when the null hypothesis is rejected to a sufficient degree. It represents the scenario where the observed results are better described by a new model, rather than by the SM alone.
- *Test Statistic* ( $Q$ ): A quantity calculated from the data sample that summarizes the information needed to make a decision about the hypotheses being tested. The test statistic is used to estimate how probable the observed result is under the null hypothesis, which helps deciding whether to reject the null hypothesis in favor of the alternative hypothesis.
- *Confidence Interval*: A range of values, derived from the data, that is believed to contain the true value of an unknown parameter with a specified probability.

- *Confidence Level (CL)*: Quantifies the degree of certainty associated with the interval estimate. It is often expressed as a percentage (e.g., 95% CL, 99% CL) and indicates the degree of certainty that a measured parameter (such as the mass of a particle or a cross-section of a process) lies within a specified range.
- *Confidence Limit*: A boundary value within a confidence interval. There are two types: the lower limit and the upper limit. These limits define the range within which the true parameter value is expected to lie with a certain CL. For example, if a measurement results in a confidence interval of [10 GeV, 20 GeV] at a 95% CL, then 10 GeV and 20 GeV are the lower and upper confidence limits, respectively. If no significant signal is observed, an upper limit is set on the parameter of interest, such as a particle's cross-section or branching ratio, to indicate the maximum value that is compatible with the observed data at a certain confidence level.

The *CLs* method [62] is a statistical technique that can be used to set upper limits on the parameter of interest, which in our case is the coupling constant of ALPs for different masses ( $g_{a\gamma}$ ). This method works by defining a test statistic to compare the signal+background with the background-only hypothesis. The observed test statistic is calculated based on our experimental data. To draw conclusions from the observed test statistic, one needs the probability density function (pdf) of the test statistic under both the null and alternative hypotheses. While this pdf can sometimes be calculated analytically, it can always be generated using Monte Carlo pseudo-experiments [58].

For convenience, the test-statistic  $Q$  is constructed to increase monotonically for increasingly signal-like (decreasingly background-like) experiments. This construction allows the confidence in the signal+background hypothesis to be quantified by the probability that the test statistic is less than or equal to the value observed in the experiment,  $Q_{obs}$ :

$$CL_{s+b} = P_{s+b}(Q \leq Q_{obs}) = \int_{-\infty}^{Q_{obs}} \frac{dP_{s+b}}{dQ} dQ, \quad (4-1)$$

where  $\frac{dP_{s+b}}{dQ}$  is the pdf of the test-statistic for signal+background experiments. Small values of  $CL_{s+b}$  indicate poor compatibility with the signal+background hypothesis and favor the background only hypothesis. Similarly, the confidence in the background hypothesis is given by the probability that the test-statistic is less than or equal to the value observed in the experiment,  $Q_{obs}$ :

$$CL_b = P_b(Q \leq Q_{obs}) = \int_{-\infty}^{Q_{obs}} \frac{dP_b}{dQ} dQ, \quad (4-2)$$

where  $\frac{dP_b}{dQ}$  is the pdf of the test-statistic for background-only experiments.

The  $CL_s$  method simply normalizes the confidence level observed for the signal+background hypothesis,  $CL_{s+b}$ , by the confidence level observed for the background-only hypothesis,  $CL_b$ :

$$CL_s \equiv \frac{CL_{s+b}}{CL_b}. \quad (4-3)$$

According to Ref. [62], this  $CL_s$  procedure provides an approximation of the confidence in the signal hypothesis,  $CL_s$ , that one might have obtained if the experiment had been conducted in the complete absence of background. Because  $CL_s$  is a ratio of confidence levels rather than a true confidence level, the method is designed to be conservative. This means that the method avoids making a claim about the presence of a signal unless there is strong evidence for it, reducing the risk of incorrectly claiming a signal where there is none. Additionally, the  $CL_s$  also addresses the undesirable property of  $CL_{s+b}$ , where two experiments with the same (small) expected signal rate but different backgrounds might yield better expected performance for the experiment with a larger background.<sup>1</sup>

For a counting experiment with observed number of events  $n_{obs}$ , the test statistic  $Q$  is often chosen as the *likelihood ratio*, which compares the likelihoods of the signal+background and background-only hypotheses given some value for the  $n_{obs}$ :

$$Q = \frac{L_{s+b}(n_{obs})}{L_b(n_{obs})}, \quad (4-4)$$

where  $L_{s+b}$  and  $L_b$  are the likelihoods under signal+background and background-only hypotheses, respectively. In this case, the likelihoods are typically Poisson distributions:

$$L_{s+b} = \frac{(s+b)^{n_{obs}} e^{-(s+b)}}{n_{obs}!}, \quad (4-5)$$

and

$$L_b = \frac{b^{n_{obs}} e^{-b}}{n_{obs}!}, \quad (4-6)$$

where  $s$  is the expected number of signal events, and  $b$  is the expected number of background events.

Thus, the likelihood ratio becomes:

$$Q = \frac{(s+b)^{n_{obs}} e^{-(s+b)}}{b^{n_{obs}} e^{-b}} = \left( \frac{s+b}{b} \right)^{n_{obs}} e^{-s}. \quad (4-7)$$

To find the distributions of  $Q$ , we need to calculate the probability of observing  $n_{obs}$  under both signal+background and background-only hypotheses. This will give  $CL_{s+b}$  and  $CL_b$ , and the ratio ( $CL_s$ ) can be computed:

---

<sup>1</sup>For further discussion on the advantages of the  $CL_s$  method, see [62].

$$CL_s = \frac{P_{s+b}(n \leq n_{obs})}{P_b(n \leq n_{obs})} = \frac{\sum_{n=0}^{n_{obs}} \frac{(s+b)^n e^{-(s+b)}}{n!}}{\sum_{n=0}^{n_{obs}} \frac{b^n e^{-b}}{n!}}. \quad (4-8)$$

To set upper limits on the parameter of interest, which in this case is the expected number of signal events,  $s$ , we vary the parameter of interest and compute  $CL_s$  for each value. Then, we determine the value of  $s$  for which  $CL_s$  is equal to the desired CL (e.g., 0.05 for 95% CL). This involves solving for the parameter value such that:

$$CL_s(s_{up}) = 0.05, \quad (4-9)$$

the value  $s_{up}$  is what we call the upper limit on the parameter of interest ( $s$ ) at 95% CL.

To illustrate the method, let's consider an example<sup>2</sup> where we observe three events ( $n_{obs} = 3$ ) with an expected background of  $b = 3.40$ , and we want to present the 95% CL upper limit on the number of signal events,  $s_{up}$ . We need to calculate the probability of observing  $n_{obs} = 3$  under both the signal+background and background-only hypotheses. This involves summing the probabilities for all possible  $n$  up to  $n_{obs} = 3$ . For the confidence level in the signal+background hypothesis:

$$CL_{s+b} = P_{s+b}(n \leq n_{obs} = 3) = \sum_{n=0}^3 \frac{(s+b)^n e^{-(s+b)}}{n!}, \quad (4-10)$$

factoring out the exponential term and expanding the sum, we get:

$$CL_{s+b} = e^{-(s+b)} \left[ 1 + (s+b) + \frac{(s+b)^2}{2} + \frac{(s+b)^3}{6} \right]. \quad (4-11)$$

By computing the above equation for 1000 values of  $s+b$  between 0 and 10, we obtain the  $CL_{s+b}$  curve shown in Fig.4.2. This curve illustrates the probability of observing three events or fewer for different values of  $s+b$ .

We can observe that when  $s+b$  is small, the probability of observing three events or less is high, close to 1. This means that for small values of  $s+b$ , it is very likely that we would observe three events or fewer, indicating good compatibility with the signal+background hypothesis. As the value of  $s+b$  increases, this probability falls, and at  $s+b = 7.75$ , the probability of observing three events or less is 5%. To find the upper limit on the signal events  $s$ , we subtract the expected background ( $b = 3.40$ ) from this value. Thus, the upper limit on  $s$  is calculated as:

$$s_{up} = 7.75 - 3.40 = 4.35. \quad (4-12)$$

Therefore, at 95% CL the upper limit on the number of signal events is  $s_{up} = 4.35$ .

---

<sup>2</sup>This example was adapted from Ref. [61].

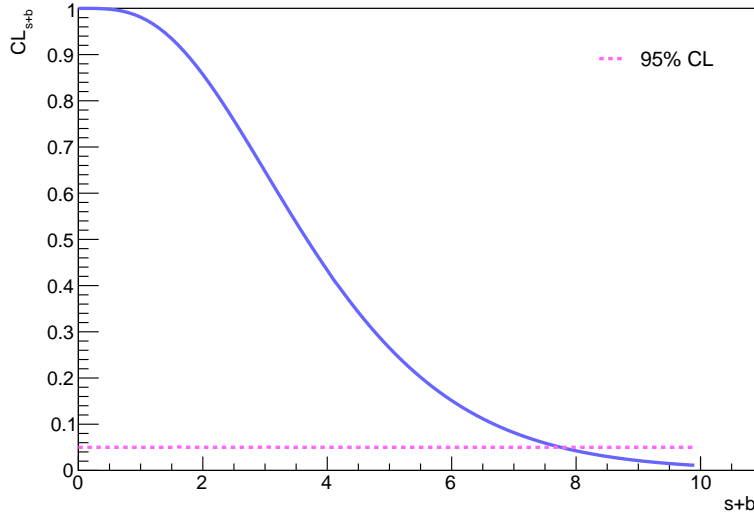


Figure 4.2: The  $CL_{s+b}$  curve for 1000 values of  $s + b$  between 0 and 10. At  $s + b = 7.75$ , the probability of observing  $n_{obs} = 3$  events or less is 5%. At this point, we can get the  $s_{up}$  from the subtraction of the given background.

As for the confidence level for the background-only hypothesis, we have:

$$CL_b = P_b(n \leq n_{obs} = 3) = \sum_{n=0}^3 \frac{(3.40)^n e^{-3.40}}{n!} \approx 0.56. \quad (4-13)$$

This calculation tells us that there is a 56% probability of observing three events or fewer under the background-only hypothesis. Now, solving  $CL_s$  for  $s + b$  such that it satisfies the following equation:

$$CL_s = \frac{CL_{s+b}}{CL_b} = \frac{e^{-(s+b)} \left[ 1 + (s+b) + \frac{(s+b)^2}{2} + \frac{(s+b)^3}{6} \right]}{0.56} = 0.05, \quad (4-14)$$

we get the green curve in Fig.4.3, which is obtained by taking the blue curve ( $CL_{s+b}$ ), normalizing it to have a maximum value of 1 in the physically sensible region (where  $s$  must be non-negative), and dividing it by 0.56. As we increase  $s + b$ , the value of  $CL_s$  decreases. When  $s + b = 8.61$ , the probability falls to 5%, this point indicates that the upper limit on  $s + b$  is 8.61 at the 95% CL. Subtracting the expected background  $b = 3.40$  from this value:

$$s_{up} = 8.61 - 3.40 = 5.21. \quad (4-15)$$

Thus, the upper limit on the number of signal events is  $s_{up} = 5.21$  at the 95% CL. This means that, based on our observations and the expected background, we can be 95% confident that the true number of signal events does not exceed 5.21. Comparing this value with the  $s_{up} = 4.35$  found using only  $CL_{s+b}$ , we see that  $CL_s$  provides a more conservative estimate.

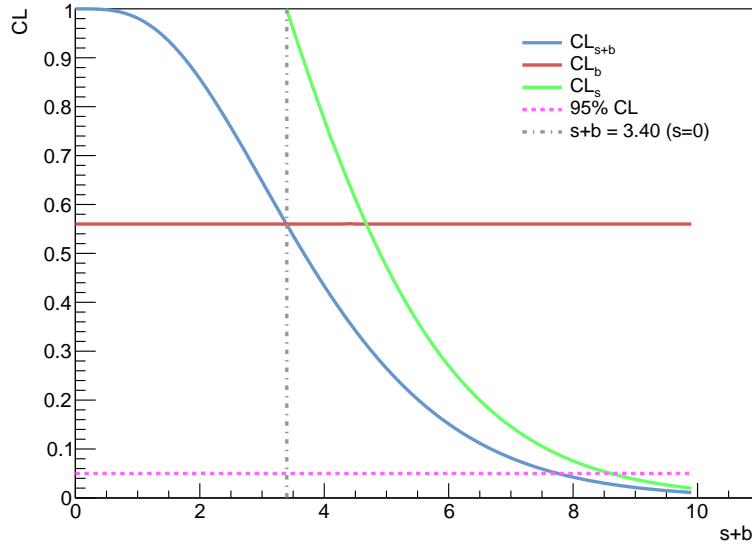


Figure 4.3: Confidence levels  $CL_{s+b}$  and  $CL_s$  for the observed number of events.

To translate the upper limit on the number of signal events ( $s_{up}$ ) into an upper limit on the coupling constant ( $g_{up}$ ), we use

$$s = \sigma_s \cdot \mathcal{L}, \quad (4-16)$$

where  $\sigma_s$  is the signal cross-section, which depends on the coupling constant, and  $\mathcal{L}$  is the integrated luminosity of the data analyzed.

The signal cross-section  $\sigma_s$  is expected to be proportional to the square of the coupling constant  $g$ :

$$\sigma_s \propto g^2. \quad (4-17)$$

Given the upper limit on the number of signal events ( $s_{up}$ ), we can find the upper limit on the coupling constant  $g_{up}$  by substituting the proportionality 4-17 into equation 4-16, resulting in

$$g_{up} \propto \sqrt{\frac{s_{up}}{\mathcal{L}}}. \quad (4-18)$$

This formula provides the upper limit on the coupling constant based on the upper limit on the number of signal events and the integrated luminosity.

#### 4.1.2

##### Definition of variables

In order to understand the selection criteria of ALP candidates in our analysis, we define the relevant variables here. These are primarily based on the topological characteristics of the ALP decay (see Fig.4.4) and particle identification. By analysing the distributions of these variables, we can better distinguish signal from background events.

The context for these variables lies in the nature of UPHIC. As discussed in Chapter 2, in UPHIC two lead nuclei pass very close to each other without directly colliding. Instead of strong hadronic interactions, their intense electromagnetic fields interact, potentially producing ALPs through photon-photon fusion ( $\gamma\gamma \rightarrow a$ ). The ALP then decays into two photons ( $a \rightarrow \gamma\gamma$ ). For most ALP masses and lifetimes considered, this production and almost immediate decay occur in the same region, typically within or very close to the VELO. The photons resulting from the ALP decay are detected in the ECAL, which is located further downstream from the VELO, as already explained in Chapter 3. Since the final state of the interaction consists of these two photons produced by the ALP decay, the relevant variables are related to the properties of these final state photons.

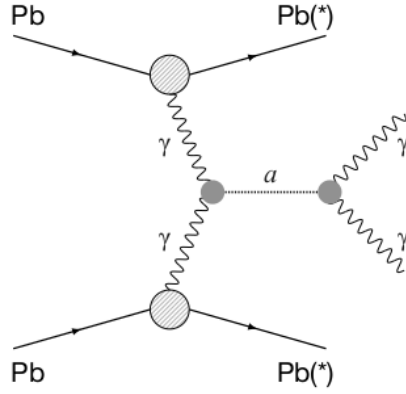


Figure 4.4: Feynman diagram of ALP production and decay in ultraperipheral PbPb collisions [9].

The key variables of the final state photons for our analysis are:

- $M_{\gamma\gamma}$ : Invariant mass combination of the two photon candidates;
- $\mathbf{p}_T(\gamma)$ : Transverse momentum of the photon candidate, which is the momentum perpendicular to the beam axis ( $z$ -axis). Its modulus is given by

$$p_T(\gamma) = \sqrt{p_x^2 + p_y^2}, \quad (4-19)$$

where  $p_x$  and  $p_y$  are the photon's components of momentum along the  $x$ -axis and  $y$ -axis, respectively;

- $\eta(\gamma)$ : Pseudorapidity (for photons is the same as the rapidity). It describes the angle of the photon candidate relative to the beam axis and is defined as

$$\eta(\gamma) = \frac{1}{2} \ln \left[ \frac{E + p_z}{E - p_z} \right], \quad (4-20)$$

where  $E$  and  $p_z$  are the photon's energy and the component of momentum along the beam axis, respectively. This variable is essential for understanding the spatial distribution of the photons;

- $\phi_\gamma$ : Azimuthal angle of the photon's momentum, which describes the angle of the photon's momentum in the transverse plane;
- $A_\phi$ : Acoplanarity between the two photon candidates. It is defined as:

$$A_\phi = 1 - \frac{\Delta\phi_{\gamma\gamma}}{\pi}, \quad (4-21)$$

where  $\Delta\phi_{\gamma\gamma}$  is the difference between the azimuthal angles of the two photons in the transverse plane ( $xy$ );

- $p_T^2(\gamma\gamma)$ : Transverse momentum squared of the diphoton system.

By carefully selecting and analyzing these variables, we can optimize the selection criteria for ALP candidates and enhance the sensitivity of our search in the ultraperipheral PbPb collisions at the LHCb experiment.

## 4.2

### Analysis samples and selection

#### 4.2.1

##### Data sample

This analysis uses data from ultraperipheral PbPb collisions at a center-of-mass energy of  $\sqrt{s} = 5.02$  TeV, recorded by the LHCb experiment during Run 2, between November and December 2018, corresponding to a integrated luminosity of  $0.216 \pm 0.09$   $nb^{-1}$ .

##### Trigger and Stripping lines

Two trigger lines at L0 hardware trigger level are used: `L0PhotonLowMult` and `L0SoftCEP`. The `L0PhotonLowMult` line, used in search studies, selects events with low multiplicity in the SPD ( $\text{Spd}(\text{Mult}) < 50$ ) and high transverse energy photons ( $\text{Photon}(E_T) > 40$  ADC).<sup>3</sup> The `L0SoftCEP` line, used to determine the efficiency of `L0PhotonLowMult`, ensures some activity in the SPD by requiring  $\text{Spd}(\text{Mult}) > 0$ , while also selecting events with a low multiplicity of hits ( $\text{Spd}(\text{Mult}) < 50$ ) and  $\text{PU}(\text{Mult}) < 255$ , thus reducing the number of pile-up events.

Events that satisfy the `L0PhotonLowMult` criteria are collected without any additional requirements in the HLT1 and HLT2 stages. Meanwhile, events that passed the `L0SoftCEP` are collected by requiring at least one VELO track ( $n_{\text{VELOtracks}} \geq 1$ ) in HLT2 (`Hlt2SingleTrack`).

---

<sup>3</sup>The ADC to  $E_T$  conversion was set to be 24 MeV/ADC

For additional refinement of event selection, the offline central production line called `StrippingHeavyIonTopologyGammaLowActivityLine` is applied. This line imposes some stringent criteria: it restricts the number of SPD hits ( $n_{\text{SPDhits}}$ ) to fewer than 2000 to minimize background from high-multiplicity events; it also limits the number of long tracks ( $n_{\text{LongTracks}}$ ), which correspond to fully reconstructed particle trajectories, to fewer than 20, and the number of VELO tracks ( $n_{\text{VELOtracks}}$ ) to fewer than 11, ensuring the selection of events with low vertex activity. These criteria collectively target low-activity events typical of ultraperipheral collisions.

The requirements for each of these lines are summarized in Table 4.1.

Line	Requirements
<code>L0PhotonLowMult</code>	$\text{Photon}(E_T) > 40$ & $\text{Spd}(\text{Mult}) < 50$
<code>L0SoftCEP</code>	$\text{Spd}(\text{Mult}) > 0$ & $\text{Spd}(\text{Mult}) < 50$ & $\text{PU}(\text{Mult}) < 255$
<code>GammaLowActivity</code>	$n_{\text{LongTracks}} < 20$ & $n_{\text{SPDhits}} < 2000$ & $n_{\text{VELOtracks}} < 11$

Table 4.1: Trigger and stripping lines requirements

#### 4.2.2

##### Monte Carlo simulation samples

Monte Carlo (MC) simulations are employed to model both the signal and background processes. The simulations can be performed using two approaches: Full Simulation and Generator Level Simulation. Full Simulation involves generating events and then passing them through a detailed simulation of the detector's response. This includes modeling the interactions of particles with the detector and the application of the same reconstruction algorithms used for real data. Full Simulation provides a realistic representation of how the detector would respond to the physical events. Generator Level Simulation, on the other hand, only models the event generation process, without simulating the detector response. The particles are generated according to the physics process being studied, but their interactions with the detector and subsequent reconstruction are not simulated. This approach is typically faster and is useful for generating large datasets or for studying processes where the detector effects are less critical.

##### Full Simulation

Events for the ALP signal production were generated using Starlight event generator [63] for ALP masses ( $m_a$ ) ranging between 3 and 10 GeV

with a mass spacing of 1 GeV. Each ALP mass sample was generated with approximately 2 million events.

Exclusive dielectron pairs from the process  $\text{Pb}+\text{Pb}(\gamma\gamma) \rightarrow \text{Pb}^{(*)}+\text{Pb}^{(*)}e^+e^-$  are used as one of the background contributions for this analysis. The process  $\gamma\gamma \rightarrow e^+e^-$  was also modelled using Starlight event generator, with  $M_{ee} > 1$  GeV. Approximately 4 million events were generated for this sample.

### Generator Level Simulation

Events for the light-by-light scattering process,  $\text{Pb}+\text{Pb}(\gamma\gamma) \rightarrow \text{Pb}^{(*)}+\text{Pb}^{(*)}(\gamma\gamma)$ , were generated using Superchic 4 [11] with  $M(\gamma\gamma) > 1$  GeV. This sample is used as another background source for this analysis, with 700 thousand events generated. However, the sample was only produced at the generator level since Superchic 4 is not yet implemented in LHCb's simulation framework. To approximate the detector effects, a smearing process was applied to the generator-level distributions, using parameters calculated from ALP events. This approach limits the ability to generate all possible distributions for the LbL background, apart from the diphoton mass, which is the primary variable of interest in this analysis.

### 4.2.3

#### Selection

In this analysis, the focus is on events with a very clean topology, where the expectation is to reconstruct only two photons and no VELO tracks. Therefore, the signal region is well defined by these two criteria:  $n_{photons} = 2$  and  $n_{VELOtracks} = 0$ . To avoid any potential bias in identifying the signal, this analysis is performed blinded in the signal region. This means that the selection criteria are established without examining the data in the invariant mass of the two photons, ensuring impartiality in the selection process [60].

To simplify the analysis, we initially considered only non-converted photons. Converted photons, which interact with the detector material to produce an electron-positron pair, require additional reconstruction steps that involve tracking these particles separately. This process introduces additional complexity and potential sources of error. Non-converted photons, detected directly in the electromagnetic calorimeter, avoid these complications. Additionally, since the photon conversion rate is 25%, the loss of statistical power is small.

Given that the trigger efficiency increases with the photon  $p_T$  and it is reasonably uniform for  $p_T(\gamma) > 1300$  MeV, this value is set as the minimum  $p_T$  requirement for the photons.

The azimuthal angle of the photons,  $\phi_\gamma$ , are also considered, as its distribution should be relatively uniform. Deviations from this expected distri-

bution can indicate the presence of electrons (from dielectron processes) that are misidentified as photons. The SMOG (System for Measuring Overlap with Gas) system [64, 65] occasionally introduces gas into the VELO region, which can cause deflections or scattering of particles. If the azimuthal angle distribution of photons is expected to be uniform, deviations could suggest that these “photons” might actually be forward electrons scattered by the gas. To reduce the influence of such background, a requirement is set to the azimuthal angle, with  $|\phi_\gamma| > 0.1$ .

With the above selection criteria, the distributions for the number of photons ( $n_{photons}$ ) and pseudorapidity,  $\eta(\gamma)$ , for both the dielectron and the 3 GeV ALP simulation samples are shown in Fig.4.5. Additionally, the distributions for acoplanarity ( $A_\phi$ ) and the transverse momentum squared of the diphoton system,  $p_T^2(\gamma\gamma)$ , are presented for events with exactly two photons ( $n_{photons} = 2$ ) and both photons within the pseudorapidity range  $2 < \eta(\gamma) < 4$ .

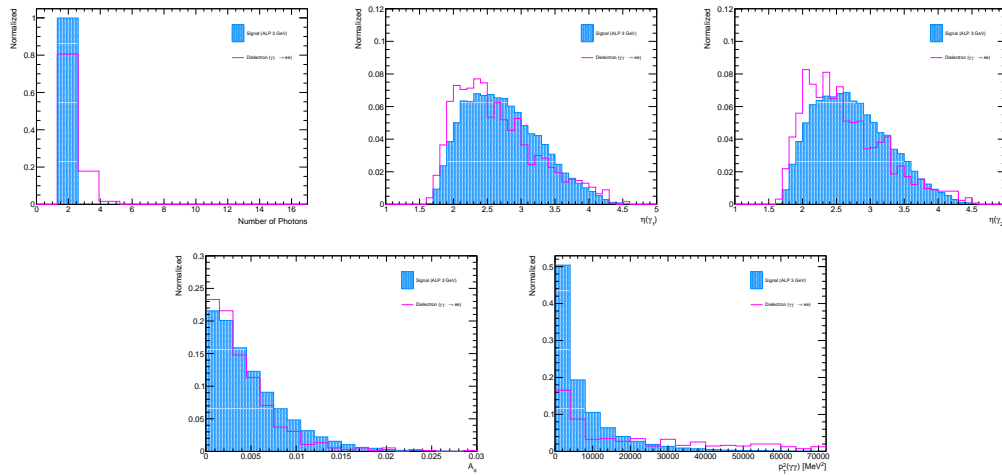


Figure 4.5: From top-left to bottom-right: number of photons, pseudorapidity, acoplanarity and diphoton  $p_T^2$  for dielectron (line-pink) and 3 GeV ALP (filled-blue) simulation samples. The requirements are explained in the text.

Photons from ALP decays are expected to be emitted back-to-back in the transverse plane, leading to low acoplanarity values. Therefore, to improve the ALP selection, two additional requirements are applied to the diphoton candidates. The value of  $p_T^2(\gamma\gamma)$  is required to be less than  $0.03 \text{ GeV}^2$  and the acoplanarity less than 0.02. While these criteria are clearly effective for signal selection, their validation across different ALP masses, not only for 3 GeV but also for 4 to 10 GeV, was performed using the Punzi Figure of Merit (Punzi FoM) [66].

The Punzi FoM is a measure designed to balance the trade-off between signal efficiency and background rejection. It accounts for both the significance

of the signal and the potential impact of background events. The figure of merit is calculated using the expression 4-22.

$$\text{PunziFoM} = \frac{\epsilon}{\frac{a}{2} + \sqrt{B}}, \quad (4-22)$$

where  $\epsilon$  is the signal efficiency,  $B$  is the expected number of background events, and  $a$  is a parameter that can be adjusted depending on the desired confidence level. Common choices for  $a$  are 3 or 5, corresponding to a  $3\sigma$  or  $5\sigma$  confidence level, respectively. In this analysis, both values of  $a$  were tested and it was observed that the Punzi FoM values varied across different ALP masses, with the optimal criteria differing slightly depending on the mass, as shown in Fig.4.6. However, to ensure consistency across the analysis, a single set of cuts was chosen,  $A_\phi < 0.02$  and  $p_T^2(\gamma\gamma) < 0.03 \text{ GeV}^2$ . By optimizing the Punzi FoM, the analysis ensures that the cuts on  $A_\phi$  and  $p_T^2(\gamma\gamma)$  are not only efficient for signal selection but also in minimizing background contamination, providing a comprehensive evaluation across all considered ALP masses.

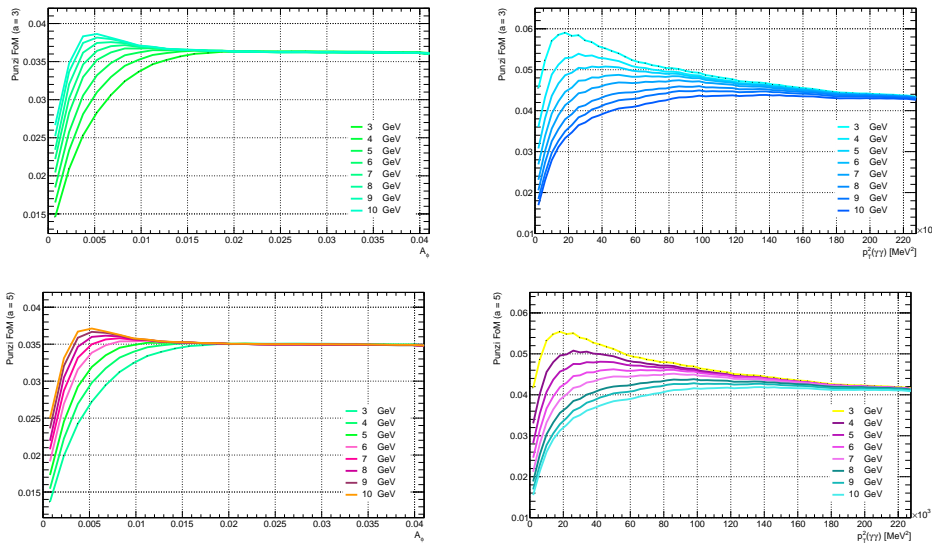


Figure 4.6: Punzi FoM for acoplanarity ( $A_\phi$ ) and diphoton transverse momentum squared ( $p_T^2(\gamma\gamma)$ ) with  $a = 3$  (top) and  $a = 5$  (bottom).

The signal efficiency for different selection values of acoplanarity and diphoton transverse momentum squared are presented in Fig.4.7. The chosen acoplanarity requirement ( $A_\phi < 0.02$ ) shows high signal efficiency across all ALP masses. On the other hand, while the selected  $p_T^2(\gamma\gamma)$  requirement ( $< 0.03 \text{ GeV}^2$ ) is not optimal for heavier ALP masses, it was chosen based on a balance between signal efficiency and background suppression, as discussed previously.

The requirements applied are:  $n_{\text{photons}} = 2$ , non-converted photons with  $p_T(\gamma) > 1300 \text{ MeV}$  and  $2 < \eta(\gamma) < 4$ .

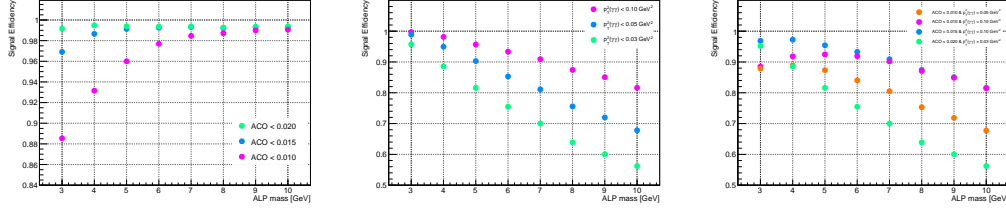


Figure 4.7: Signal efficiencies for different selection values of acoplanarity (left), diphoton transverse momentum squared (middle), and the combination of both (right)

Finally, Fig.4.8 presents distributions of the number of VELO tracks ( $n_{VELOtracks}$ ), the transverse momentum of each photon,  $p_T(\gamma_1)$  and  $p_T(\gamma_2)$ , and the invariant mass of the diphoton system ( $M_{\gamma\gamma}$ ) for candidates meeting all the selection criteria outlined (see Table 4.2). It is clear that applying the  $n_{VELOtracks} = 0$  requirement completely eliminates the dielectron simulation sample events. Although this criterion was expected to reduce the dielectron background, applying  $n_{VELOtracks} = 0$  does not provide meaningful results due to the insufficient statistics of the dielectron sample. Additionally, as will be shown in the next section, the shape of the dielectron mass distribution appears to be independent of the number of VELO tracks. Therefore, in the absence of events with no tracks, the shape obtained from events with  $n_{VELOtracks} > 0$  can be utilized to predict the background shape in the signal region.

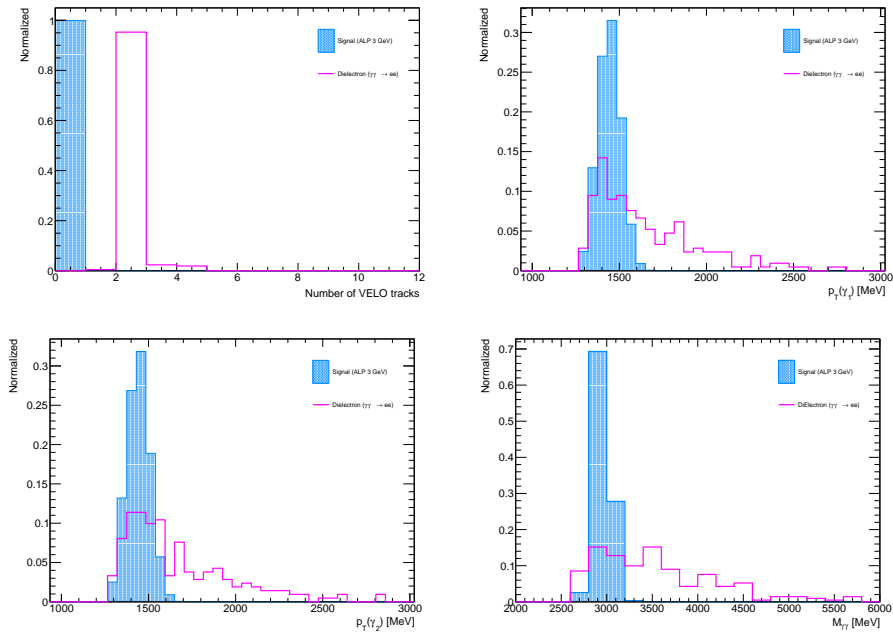


Figure 4.8: From top-left to bottom-right:  $n_{VELOtracks}$ , diphoton mass, photon's  $p_T$  distributions for dielectron (line-pink) and 3 GeV ALP (filled-blue) simulation samples. The requirements are explained in the text.

Summary Selection
Non-converted photons
$n_{photons} = 2$
$p_T(\gamma) > 1300 \text{ MeV}$
$2 < \eta(\gamma) < 4$
$ \phi_\gamma  > 0.1$
$p_T^2(\gamma\gamma) < 0.03 \text{ GeV}^2$
$A_\phi < 0.02$

Table 4.2: Selection criteria for the diphoton candidates

#### 4.2.4 Trigger and HeRSChel Efficiencies

The trigger efficiency was determined using the tag-and-probe method, a data-driven technique for measuring particle detection efficiencies based on the decays of known resonances to pairs of the particles being studied. In this analysis, these particles are photons ( $\gamma\gamma$ ), and the  $\eta$  and  $\pi^0$  resonances are used. The efficiency ( $\epsilon$ ) is calculated by comparing the number of diphoton candidates that pass the L0 trigger selection ( $n^p$ ) to the total number of candidates, which includes both those that pass and those that fail the selection ( $n^p + n^f$ ):  $\epsilon = \frac{n^p}{n^p + n^f}$ .

For photons originating from  $\eta$  and  $\pi^0$  decays, the trigger efficiency reaches a plateau for  $p_T > 1300 \text{ MeV}$ , as shown in Fig.4.9 where the combined efficiency for these photons is found to be  $58.6 \pm 0.4\%$ .

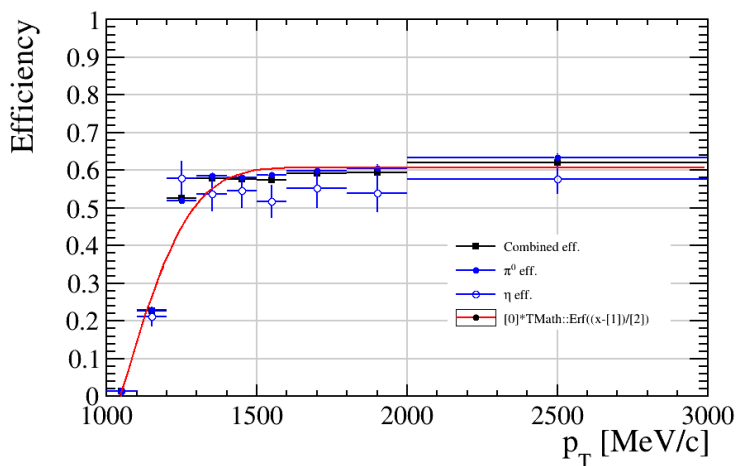


Figure 4.9: Efficiency results as a function of transverse momentum using the tag-and-probe method based on the decays of  $\eta$  and  $\pi^0$  resonances to pairs of photons.

To account for the fact that the analysis involves selecting events with two photons, the overall trigger efficiency used is given by:

The HeRSChel detector can be used to effectively suppress high multiplicity background at very forward region. A requirement on the HeRSChel variable,  $\log(\chi_{HRC}^2) < 8.35$  (Fig.4.10), has been applied to eliminate almost 100% of these background while maintaining a signal efficiency of approximately 90%. As detailed in Ref. [57] this specific cut results in an estimated efficiency of:

$$\epsilon_{HRC}(\log(\chi_{HRC}^2) < 8.35) = (90.1 \pm 1.2)\%. \quad (4-23)$$

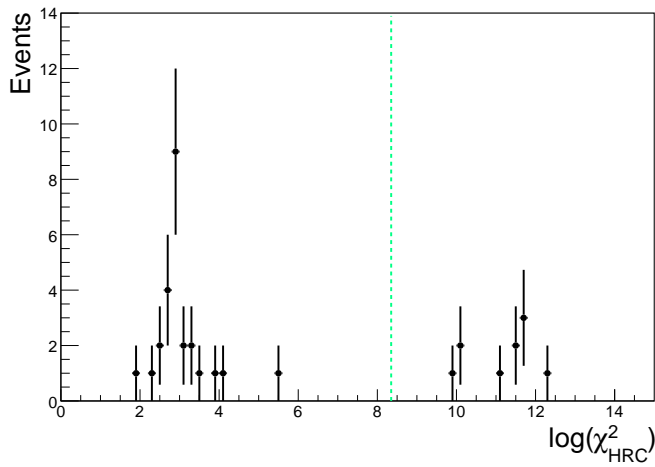


Figure 4.10: Distribution for the HeRSChel variable for data,  $\log(\chi_{HRC}^2)$ . The green line represents the cut in 8.35 considered for calculate the HeRSChel efficiency. The selection criteria for this sample is the same as in table 4.2, including the L0PhotonLowMult trigger requirements and  $n_{VELOtracks} \geq 1$ .

## 4.3

### Signal and Background estimations

#### 4.3.1

##### MC ALP signal yield

The expected number of ALP events,  $n_{exp}$ , is determined by

$$n_{exp} = n_{sel} \times w_{alp}, \quad (4-24)$$

where  $n_{sel}$  is the number of ALP events remaining after applying all the selection criteria described in the previous section (Table 4.2, including  $n_{VELOtracks} = 0$ ), and the weight factor  $w_{alp}$  is calculated as follows

$$w_{alp} = \frac{\mathcal{L} \times \sigma_{\gamma\gamma \rightarrow a \rightarrow \gamma\gamma} \times \epsilon_{trig} \times \epsilon_{HRC}}{n_{gen,ALP}} \times \frac{g_{ALP}^2}{(10^{-3})^2}, \quad (4-25)$$

where  $\mathcal{L} = 0.216 \text{ nb}^{-1}$  is the integrated luminosity,  $\sigma_{\gamma\gamma \rightarrow a \rightarrow \gamma\gamma}$  is the predicted cross-section for an ALP mass hypothesis with  $g_{ALP} = 10^{-3}$ ,  $\epsilon_{trigger}$  and  $\epsilon_{HRC}$  are the trigger and HeRSChel efficiencies provided by Eq.?? and Eq.4-23, respectively.  $n_{gen,ALP}$  is the number of generated events for that ALP mass, and  $g_{ALPnorm}$  is a normalization factor that accounts for the fact that the ALP cross-section,  $\sigma_{\gamma\gamma \rightarrow a \rightarrow \gamma\gamma}$ , is calculated with  $g_{ALP} = 10^{-3}$ .

For instance, for an ALP mass hypothesis of 3 GeV, 2,036,652 events were generated ( $n_{gen,ALP}$ ), with a predicted cross-section of  $\sigma_{\gamma\gamma \rightarrow a \rightarrow \gamma\gamma} = 1.27 \times 10^4 \text{ nb}$  [11]. This results in a weight factor of  $w_{alp} = 1.01 \times 10^{-5}$ . After applying the selection criteria, 37,262 events remain ( $n_{sel}$ ), leading to an expected number of 3 GeV ALP events of:

$$n_{exp}(3 \text{ GeV}) = 37,262 \times 1.01 \times 10^{-5} \approx 0.38. \quad (4-26)$$

Similarly, the expected number of ALP events for each of the studied mass hypotheses has been calculated and are summarized in Table 4.3.

mass [GeV]	$\sigma_{\gamma\gamma \rightarrow a \rightarrow \gamma\gamma}$ [nb]	$n_{gen,ALP}$	$n_{sel}$	$n_{exp}$
3	$1.27 \times 10^4$	2,036,652	37,262	0.38
4	$8.73 \times 10^3$	2,713,257	49,082	0.26
5	$7.17 \times 10^3$	2,293,087	34,476	0.17
6	$7.17 \times 10^3$	2,055,123	25,375	0.14
7	$6.21 \times 10^3$	2,237,143	23,073	0.10
8	$5.44 \times 10^3$	2,204,730	18,556	0.07
9	$4.82 \times 10^3$	2,205,091	15,732	0.06
10	$4.31 \times 10^3$	2,164,133	12,860	0.04

Table 4.3: Expected number of ALP candidates ( $n_{exp}$ ) for different mass hypotheses, after applying the selection criteria. The table also shows the predicted cross-sections ( $\sigma_{\gamma\gamma \rightarrow a \rightarrow \gamma\gamma}$ ) [11], the number of generated events ( $n_{gen,ALP}$ ), and the number of events remaining after the selection ( $n_{sel}$ ).

### 4.3.2

#### Light-by-Light background

Light-by-Light (LbL) scattering, where two photons interact and produce another pair of photons, is a process that can mimic the signal of ALPs in ultraperipheral PbPb collisions. This process can produce events that are indistinguishable from ALP decays in the detector, making it a potentially significant background in the search for ALPs.

The predicted cross-section for LbL scattering with  $M_{\gamma\gamma} > 1 \text{ GeV}$  is  $\sigma_{\gamma\gamma \rightarrow \gamma\gamma} = 1.37 \times 10^4 \text{ nb}$  [11], corresponding to 2,964 expected events in the

data set used for this analysis, based on the integrated luminosity ( $\mathcal{L} = 0.216 \text{ nb}^{-1}$ ).

As previously discussed, 700,000 events were generated ( $n_{gen,LbL}$ ) at generator level. Within the LHCb acceptance, 23.46 events ( $n_{sel}$ ) from the simulation pass the requirements of the signal region (Table 4.2, including  $n_{VELOtracks} = 0$ ). The weight factor,  $w_{LbL}$ , is then calculated as:

$$w_{LbL} = \frac{\mathcal{L} \times \sigma_{\gamma\gamma \rightarrow \gamma\gamma} \times \epsilon_{trig} \times \epsilon_{hrc}}{n_{gen,LbL}} \approx 0.003. \quad (4-27)$$

Resulting in  $n_{exp} = n_{sel} \times w_{LbL} = 0.07$  expected events for the LbL background.

### 4.3.3

#### Dielectron background

The dielectron background arises when two electrons produced in ultra-peripheral collisions are misidentified as photons, with no VELO tracks reconstructed. Although the high VELO tracking efficiency significantly suppresses this background, the dielectron production cross-section is much larger than the ALP signal, estimated to be  $\sigma_{\gamma\gamma \rightarrow e^+e^-} = 2.68 \times 10^6 \text{ nb}$  [11] for an invariant mass greater than 1 GeV. This results in approximately 580,000 dielectron events for the 2018 PbPb data. After generating  $n_{gen,dielectron} = 4 \times 10^6$  dielectron events using the Starlight generator and applying the selection criteria in Table 4.2, 211 events remain. However, as shown in Fig.4.8, no dielectron candidates survive after imposing the  $n_{VELOtracks} = 0$  requirement.

Given the absence of dielectron candidates in the signal region, requesting additional simulation events could theoretically improve the estimate. However, the number of events required to obtain a statistically meaningful distribution would be unreasonably high. Therefore, an alternative method is proposed to estimate both the background yield and the shape of the  $M_{\gamma\gamma}$  distribution. If the shape of the dielectron  $M_{\gamma\gamma}$  distribution is independent of  $n_{VELOtracks}$ , we can use the shape obtained from events with tracks to predict the distribution for the  $n_{VELOtracks} = 0$  case. As indicated in Fig.4.8, most dielectron events contain two VELO tracks. To verify whether this background sample accurately describes the data, a control sample was defined.

#### 4.3.3.1

##### Dielectron control sample

To validate the simulation modeling of the dielectron background, a dielectron-enriched control sample is defined. This control sample is selected using the same criteria as in Table 4.2, with the additional requirement of  $n_{VELOtracks} = 2$ . In the data, events in the control sample must also pass the

L0PhotonLowMult trigger, with at least one of the photons satisfying this trigger. The HeRSChel variable is constrained by  $\log(\chi_{\text{HRC}}^2) < 8.35$  and the simulation is corrected to account for the HeRSChel and trigger efficiencies.

For this control sample, 15 events are observed in the data. After applying the selection criteria to the dielectron simulation sample, 201 events remain, resulting in an expected number of events,  $n_{exp}$ , calculated as:

$$n_{exp} = 201 \times w_{dielectron} \approx 21.7, \quad (4-28)$$

where the weight factor  $w_{dielectron}$  is given by:

$$w_{dielectron} = \frac{\mathcal{L} \times \sigma_{\gamma\gamma \rightarrow e^+e^-} \times \epsilon_{trig} \times \epsilon_{hrc}}{n_{gen,dielectron}} \approx 0.108. \quad (4-29)$$

The distributions of  $n_{VELOtracks}$  and  $n_{photons}$  in the data are well described by the simulation, as shown in Fig.4.11.

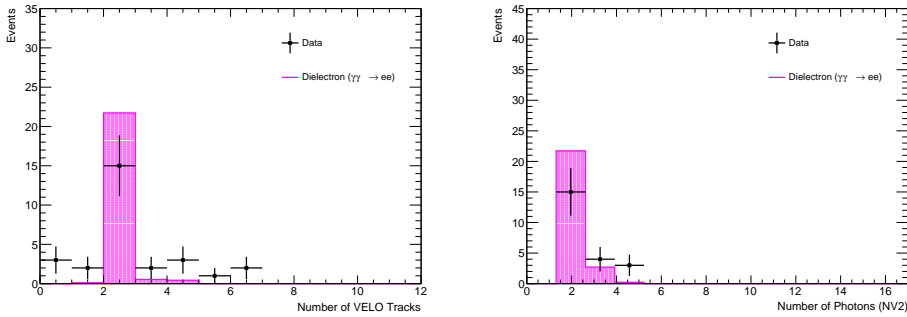


Figure 4.11: Distribution of the number of VELO tracks (left) and the number of photons (right) for the dielectron control sample.

The distributions of the diphoton invariant mass, photon  $p_T$ , diphoton acoplanarity, diphoton  $p_T^2$ , photon pseudorapidity, and azimuthal angles (Figures: 4.12, 4.13, 4.14, 4.15) are also compared and found to be reasonably described by simulation. For these distributions, the figures also show the corresponding distributions without the  $n_{photons} = 2$  requirement to enhance statistics. Overall, the good agreement between data and simulation suggests that the dielectron background is accurately modeled.

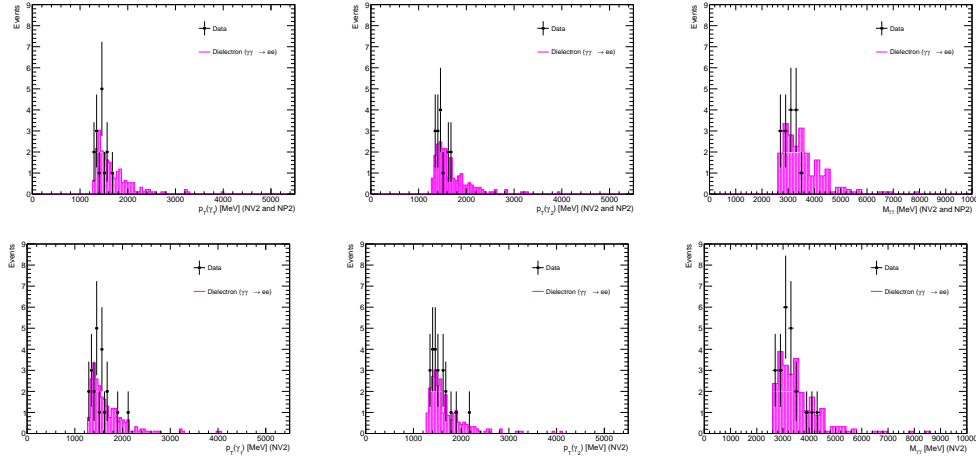


Figure 4.12: Distributions of the photon transverse momentum ( $p_T$ ) for both photons, and the diphoton invariant mass (top right) in the dielectron control sample. The bottom row shows the same distributions without the  $n_{photons} = 2$  requirement.

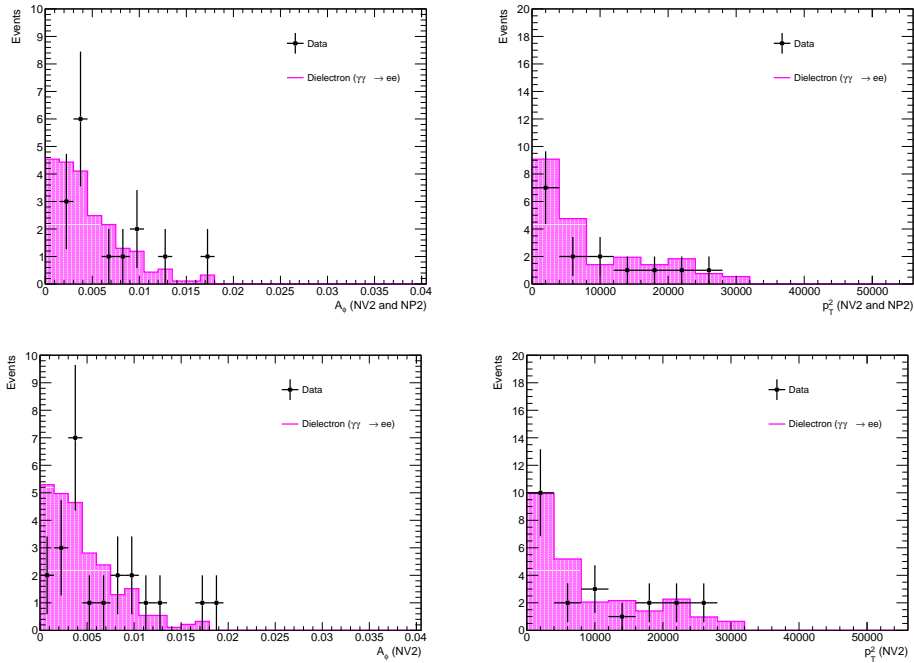


Figure 4.13: Distributions of the diphoton acoplanarity (left) and the diphoton transverse momentum squared ( $p_T^2$ ) (right) in the dielectron control sample. The bottom row shows the same distributions without the  $n_{photons} = 2$  requirement.

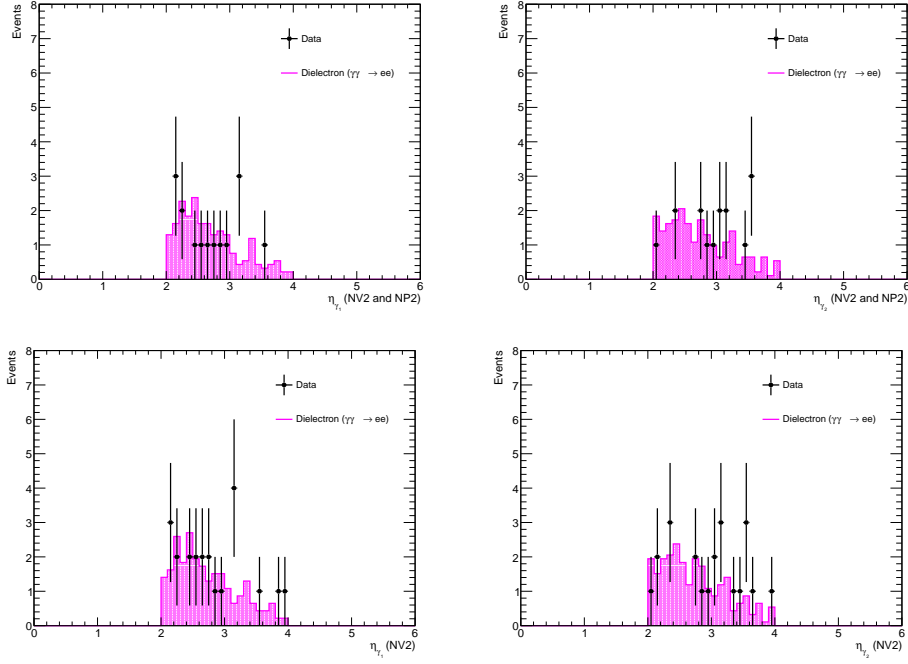


Figure 4.14: Distributions of the pseudorapidity for the leading photon (left) and subleading photon (right) in the dielectron control sample. The bottom row shows the same distributions without the  $n_{photons} = 2$  requirement.

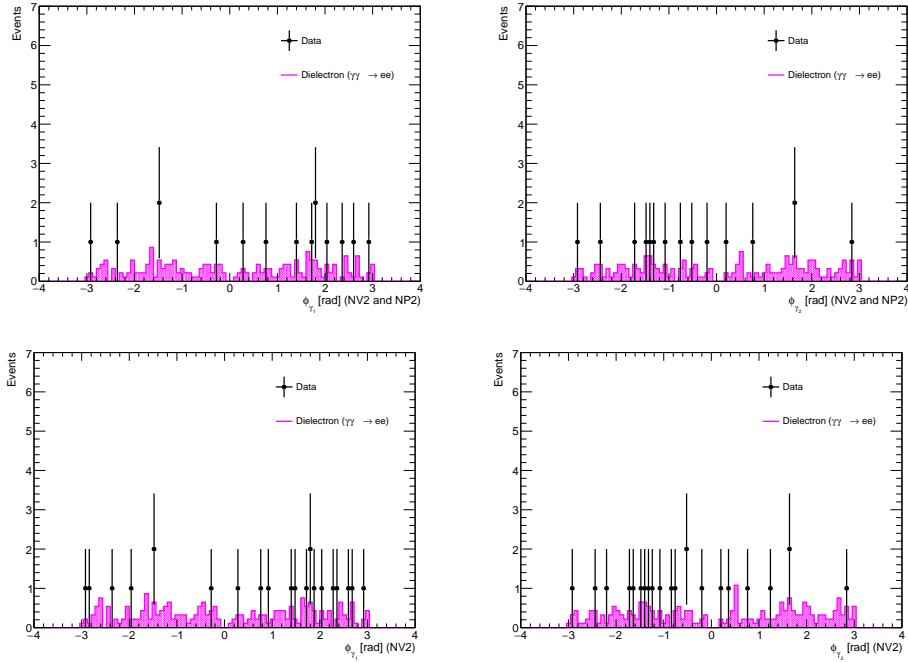


Figure 4.15: Distributions of the azimuthal angle for the leading photon (left) and subleading photon (right) in the dielectron control sample. The bottom row shows the same distributions without the  $n_{photons} = 2$  requirement.

### 4.3.3.2 Dielectron shape

Since, in simulation, there is no dielectron events in the signal region (with  $n_{VELOtracks} = 0$ ), it is necessary to study the dielectron mass distribution to demonstrate that its shape does not depend on the number of VELO tracks. This is important because, without dielectron events in the signal region, we must rely on events from other regions (with different numbers of VELO tracks) to model the dielectron background shape.

To validate this, the dielectron mass distribution is compared for events with  $n_{VELOtracks} = 2$  and those with  $n_{VELOtracks} = 1, 3, \text{ or } 4$ . As shown in Fig.4.16, the distribution for  $n_{VELOtracks} = 1, 3, \text{ or } 4$  has limited statistics. To improve the statistical significance, the requirements on  $n_{photons} = 2$  and  $p_T^2(\gamma\gamma) > 0.03 \text{ GeV}^2$  were relaxed (Fig.4.16, right). These distributions are consistent, indicating that the shape of the dielectron mass distribution seems to be independent of the number of VELO tracks.

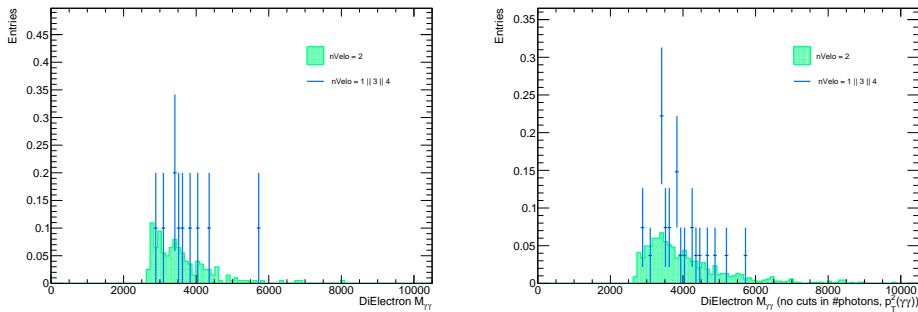


Figure 4.16: Shape comparison between two different selections for the dielectron simulation. As explained in the text,  $n_{VELOtracks} = 1$  or  $3$  or  $4$  (blue points) and  $n_{VELOtracks} = 2$  (filled-green) have similar shapes. The bottom plot exclude the  $n_{photons} = 2$  and  $p_T^2(\gamma\gamma) > 0.03 \text{ GeV}^2$  criteria in order to enhance the statistics.

This allows us to estimate the expected number of dielectron events in the signal region by using the dielectron  $M_{\gamma\gamma}$  shape that satisfies all other selection criteria except for the requirement of  $n_{VELOtracks} = 0$ . Since the upper limit on the number of events is 3 when no events are observed, the shape is scaled to have  $n_{sel} = 3$ . The expected number of dielectron background events,  $n_{exp}$ , is then calculated as:

$$n_{exp} = 3 \times w_{dielectron} \approx 0.32. \quad (4-30)$$

## 4.4 Results and Discussion

This section presents the expected  $CLs$  limits on the ALP-photon coupling constant,  $g_{a\gamma}$ , for ALPs with masses ranging from 3 to 10 GeV. The search for the  $\gamma\gamma \rightarrow a \rightarrow \gamma\gamma$  process is conducted using the diphoton invariant mass distribution, with LbL scattering and dielectron processes considered as the main background contributions.

### 4.4.1 Expected $CLs$ limits

The estimated number of background events in the signal region is 0.07 for the LbL and 0.32 for the dielectron. The ALP signal, generated using Monte Carlo simulations with Starlight generator, models masses between 3 and 10 GeV. The expected number of ALP signal events for each mass hypothesis is summarized in Table 4.3.

The diphoton invariant mass distribution for two representative ALP mass hypotheses, 3 GeV and 5 GeV, including both background contributions are shown in Fig.4.17. These distributions provide a comparison basis for the observed data after unblinding.

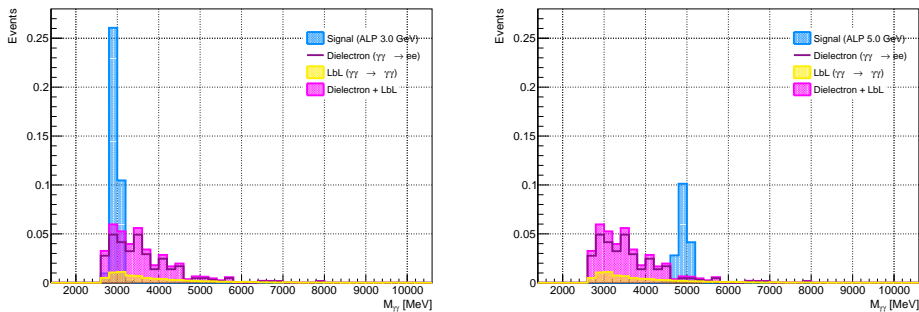


Figure 4.17: Diphoton invariant mass distribution for the ALP signal with mass hypotheses of 3 GeV (left) and 5 GeV (right). The distributions combine the expected ALP signal with background contributions.

In order to set upper limits in the ALP-photon coupling constant, we assume that no data events are observed in the signal region,  $n_{obs} = 0$ . The 95% confidence level (CL) upper limits on  $g_{a\gamma}$  are calculated using the  $CLs$  method, implemented via the TLimit [67] class from the ROOT framework. The implementation involves iterating over a range of  $g_{a\gamma}$  values, scaling the ALP signal accordingly (proportionally to  $g^2$ ), and using the TLimitDataSource class to pass the signal and background histograms to the TLimit.ComputeLimit method. This method returns the expected  $CLs$

value for each  $g_{a\gamma}$ , which is then used to generate the  $CLs$  curves, as shown in Fig.4.18 for 3 GeV and 5 GeV mass hypotheses. Although TLimit is considered legacy code, it effectively serves this analysis needs. For future work, especially when incorporating systematic uncertainties, more recent tools such as HistFactory [68], RooFit [69], and RooStats [70] could offer enhanced flexibility and accuracy.

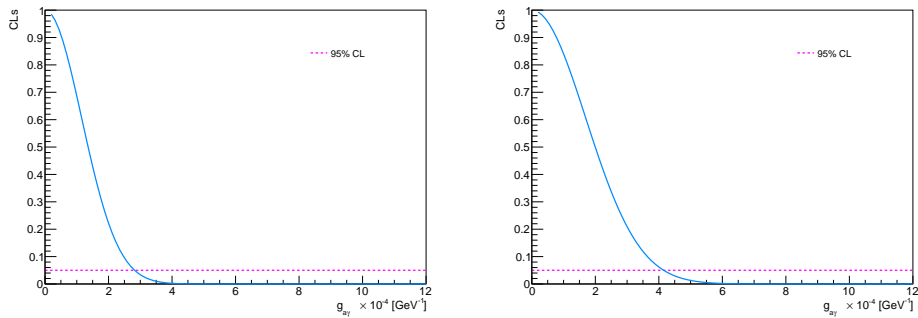


Figure 4.18:  $CLs$  limits for ALP mass hypotheses of 3 GeV (left) and 5 GeV (right) using the TLimit class from the ROOT framework. These curves show the expected exclusion limits for the ALP-photon coupling constant at 95% CL (light pink dashed line).

The upper limits on  $g_{a\gamma}$  for all tested mass hypotheses are summarized in Table 4.4.

mass [GeV]	upper limit in $g_{a\gamma}$ [ $\text{TeV}^{-1}$ ]
3	0.28
4	0.34
5	0.42
6	0.46
7	0.54
8	0.64
9	0.73
10	0.85

Table 4.4: Upper limits on the ALP-photon coupling constant  $g_{a\gamma}$  for different ALP mass hypotheses, calculated using the  $CLs$  method. These limits do not account for systematic uncertainties.

#### 4.4.2 Exclusion Region

The limits in table 4.4 are then used to construct an expected exclusion region in the  $(g_{a\gamma}, m)$  parameter space, shown in Fig.4.19.

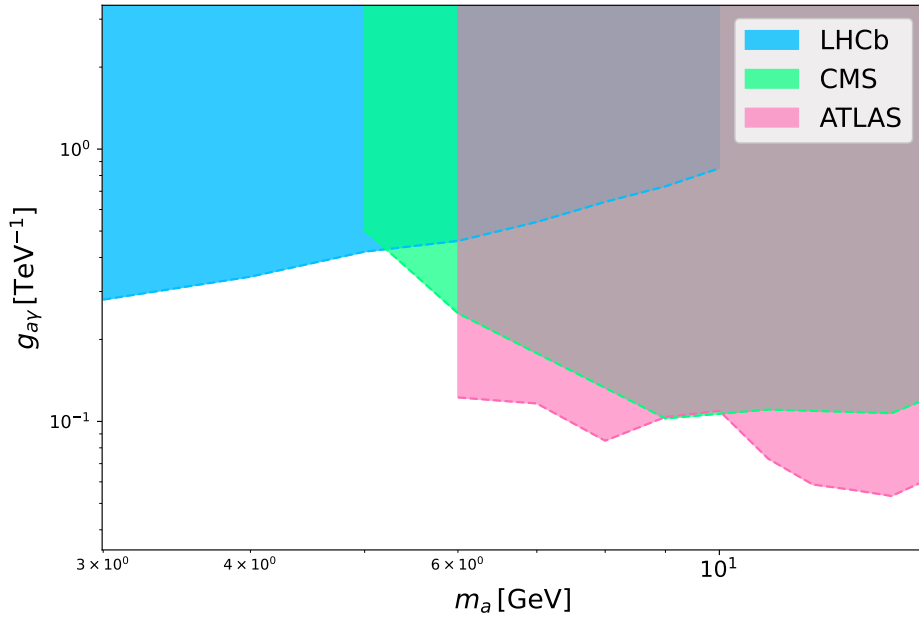


Figure 4.19: Exclusion region in the  $g_{a\gamma}$  versus ALP mass plane, representing the values excluded at 95% CL for the tested mass range, compared with the exclusion limits obtained by ATLAS [9] and CMS [8] experiments.

This exclusion region illustrates the 95% CL excluded values of  $g_{a\gamma}$  across the ALP mass range of 3 to 10 GeV. For higher masses, the sensitivity of the analysis decreases, leading to less stringent exclusions for  $g_{a\gamma}$ . For instance, for a 3 GeV ALP, the upper limit on  $g_{a\gamma}$  is  $0.28 \text{ TeV}^{-1}$ , excluding all values above that, while for a 10 GeV ALP, the upper limit is less stringent, excluding values above  $0.85 \text{ TeV}^{-1}$ . To provide context, our results are compared with the exclusion limits obtained by the ATLAS [9] and CMS [8]. Notably, our analysis yields stronger constraints for ALP masses  $m_a \leq 5 \text{ GeV}$ .

## 5

### Conclusions and Future Prospects

This dissertation reported the analysis on the search for ALPs in ultraperipheral PbPb collisions using data collected by the LHCb experiment during Run 2 (2018). The analysis focused on ALPs that couple exclusively to photons, investigating the process:  $\text{Pb} + \text{Pb} (\gamma\gamma) \rightarrow a \rightarrow \text{Pb}^{(*)} + \text{Pb}^{(*)}\gamma\gamma$ . Ultraperipheral heavy ion collisions (UPHIC) were selected for their favorable conditions in studying ALPs that couple exclusively to photons. The aim of this work was to set expected upper limits on the ALP-photon couplings,  $g_{a\gamma}$ , for ALP masses ranging from 3 to 10 GeV—a mass range challenging for other detectors.

This analysis was performed blinded to prevent bias, ensuring that the selection of data in the signal region was not influenced by the data itself. The results presented serve as a strategic framework for the analysis that, if approved by the collaboration, will be applied to unblinded data to obtain the final results.

The expected number of signal events for each ALP mass hypothesis was estimated using full simulation. Two sources of background were considered for this analysis: light-by-light (LbL) scattering and dielectron processes. The LbL background was estimated from generator level simulations, while the dielectron background was modeled using full simulation. The shape of the dielectron mass distribution from events with VELO tracks was employed to predict the background in the signal region, defined by events with no VELO tracks. Additionally, a dielectron control sample was used to validate the simulation modeling of this background.

The analysis covered an ALP mass range from 3 to 10 GeV and  $g_{a\gamma}$  values from  $0.28 \text{ TeV}^{-1}$  to  $0.85 \text{ TeV}^{-1}$  in the  $(g_{a\gamma}, m)$  parameter space. Although the exclusion region identified is relatively small, this is the first investigation of its kind at LHCb focusing on ALPs in ultraperipheral PbPb collisions. The results highlight LHCb's potential to contribute to ALP searches in future runs, particularly with the increased data in Run 3.

This work also contributed to the study of the software trigger implemented in Run 3 (2023), which outperforms the hardware trigger used in Run 2. The comparison between the acoplanarity distribution is shown in Fig.5.1-left, where one can see that 2023 data has higher purity for UPC diphoton production. The photon  $E_T$  distribution is shown in Fig.5.1-right with a clear observation that in 2023 data, the trigger had higher efficiency for low- $E_T$  pho-

tons which means that studies of low-mass resonances can now be performed with this new data set.

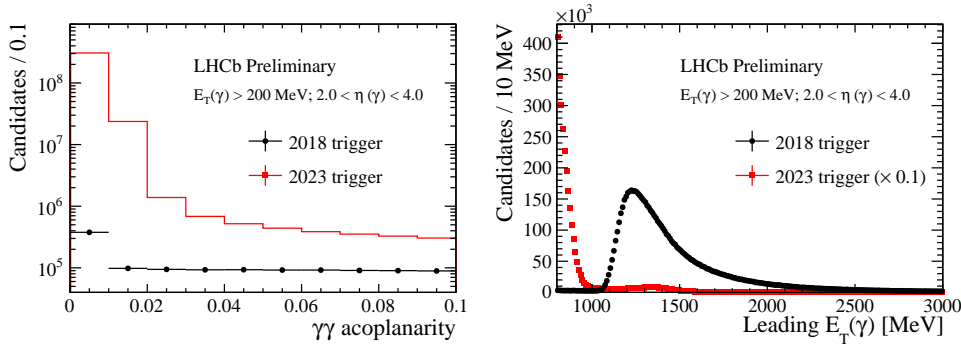


Figure 5.1: Left: Acoplanarity of the photon pairs. Right: Leading photon  $E_T$  photon pairs. Both for data taken in 2018 and 2023. In 2018, the photon pairs are selected with a hardware trigger while for 2023 data set, they are selected with a software trigger implemented in GPUs. Taken from ref [10]

### Next steps

The next steps in this analysis involve the inclusion of systematic uncertainties, which are critical for accurately interpreting the results and setting robust exclusion limits. Additionally, the contribution from the  $gg \rightarrow \gamma\gamma$  background will be incorporated. This background arises from the exclusive diphoton final state produced via strong interaction through a quark loop in the exchange of two gluons. Although this background is not expected to have a significant impact, its inclusion will provide a more comprehensive estimation. Further, a study of other possible sources of background will be undertaken to ensure all relevant contributions are accounted for in the analysis. The CLs calculations, currently performed using the TLimit class from the ROOT framework, will be updated using more modern tools such as HistFactory, RooFit, and RooStats. The final task will be to complete the analysis note.

## 6

### Bibliography

- 1 BALTZ, A. et al. The physics of ultraperipheral collisions at the LHC. *Physics Reports*, Elsevier, v. 458, n. 1-3, p. 1–171, 2008. Cited 4 times in pages 8, 14, 22, and 23.
- 2 GONCALVES, V.; MARTINS, D.; RANGEL, M. Searching for axionlike particles with low masses in pPb and PbPb collisions. *The European Physical Journal C*, Springer, v. 81, n. 6, p. 1–8, 2021. Cited 3 times in pages 8, 24, and 27.
- 3 D'ENTERRIA, D. Collider constraints on axion-like particles. *arXiv preprint arXiv:2102.08971*, 2021. Cited 5 times in pages 8, 13, 24, 25, and 26.
- 4 BETETA, C. A. et al. Calibration and performance of the LHCb calorimeters in run 1 and 2 at the LHC. *arXiv preprint arXiv:2008.11556*, 2020. Cited 4 times in pages 8, 30, 34, and 35.
- 5 LHCb Collaboration ALVES JR, A. A. et al. The LHCb detector at the LHC. *Journal of Instrumentation*, IOP Publishing, v. 3, n. 08, p. S08005, 2008. Cited 4 times in pages 8, 28, 29, and 32.
- 6 DALL'OCCO, E. *Search for heavy neutrinos and characterisation of silicon sensors for the VELO upgrade*. Tese (Doutorado) — Ph. D. thesis, Universiteit Amsterdam, 2020. Cited 2 times in pages 8 and 35.
- 7 AKIBA, K. C. et al. The HeRSChel detector: high-rapidity shower counters for LHCb. *Journal of Instrumentation*, IOP Publishing, v. 13, n. 04, p. P04017, 2018. Cited 4 times in pages 8, 31, 38, and 39.
- 8 CMS Collaboration BELFORTE, S. et al. Evidence for light-by-light scattering and searches for axion-like particles in ultraperipheral PbPb collisions at  $\sqrt{s_{NN}} = 5.02$  TeV. *Physics Letters. Section B*, v. 797, p. 1–27, 2019. Cited 6 times in pages 9, 10, 26, 40, 41, and 64.
- 9 ATLAS Collaboration GONCALO, R. et al. Measurement of light-by-light scattering and search for axion-like particles with 2.2 nb<sup>-1</sup> of Pb + Pb data with the ATLAS detector. *Journal of High Energy Physics*, Springer Nature, v. 2021, n. 3, p. 243, 2021. Cited 7 times in pages 9, 10, 22, 26, 40, 47, and 64.
- 10 LHCb Collaboration. Photon triggers for ultra-peripheral lead-lead collisions in run 2 and run 3. 2024. Disponível em: <<https://cds.cern.ch/record/2898822>>. Cited 2 times in pages 10 and 66.
- 11 HARLAND-LANG, L. et al. A new approach to modelling elastic and inelastic photon-initiated production at the LHC: SuperChic 4. *The European Physical Journal C*, Springer, v. 80, p. 1–14, 2020. Cited 4 times in pages 11, 50, 56, and 57.

- 12 ARUN, K.; GUDENNAVAR, S.; SIVARAM, C. Dark matter, dark energy, and alternate models: A review. *Advances in Space Research*, Elsevier, v. 60, n. 1, p. 166–186, 2017. Cited 2 times in pages 13 and 18.
- 13 Planck Collaboration ADE, P. et al. Planck 2013 results. XVI. cosmological parameters. *A&A*, v. 571, p. A16, 2014. Cited 2 times in pages 13 and 18.
- 14 FISHER, P.; KAYSER, B.; MCFARLAND, K. S. Neutrino mass and oscillation. *Annual Review of Nuclear and Particle Science*, Annual Reviews 4139 El Camino Way, PO Box 10139, Palo Alto, CA 94303-0139, USA, v. 49, n. 1, p. 481–527, 1999. Cited 2 times in pages 13 and 18.
- 15 CANETTI, L.; DREWES, M.; SHAPOSHNIKOV, M. Matter and Antimatter in the Universe. *New Journal of Physics*, IOP Publishing, v. 14, n. 9, p. 095012, 2012. Cited 2 times in pages 13 and 18.
- 16 ROSNER, J. L. CP violation—a brief review. In: *AIP Conference Proceedings*. [S.l.: s.n.], 2000. v. 540, n. 1, p. 283–304. Cited 2 times in pages 13 and 18.
- 17 HOOFT, G. 't. Symmetry breaking through Bell-Jackiw anomalies. *Physical Review Letters*, v. 37, n. 1, p. 8–11, 1976. Cited 2 times in pages 13 and 19.
- 18 PECCEI, R. D. The strong CP problem and axions. In: *Axions: Theory, Cosmology, and Experimental Searches*. [S.l.]: Springer, 2008. p. 3–17. Cited 2 times in pages 13 and 20.
- 19 PECCEI, R. D.; QUINN, H. R. CP conservation in the presence of pseudoparticles. *Physical Review Letters*, APS, v. 38, n. 25, p. 1440, 1977. Cited 2 times in pages 13 and 20.
- 20 IRASTORZA, I. G.; REDONDO, J. New experimental approaches in the search for axion-like particles. *Progress in Particle and Nuclear Physics*, Elsevier, v. 102, p. 89–159, 2018. Cited 2 times in pages 13 and 21.
- 21 COELHO, R. et al. Production of axionlike particles in PbPb collisions at the LHC, HE-LHC and FCC: A phenomenological analysis. *Physics Letters B*, Elsevier, v. 806, p. 135512, 2020. Cited 3 times in pages 14, 23, and 27.
- 22 ATLAS Collaboration AAD, G. et al. *The ATLAS experiment at the CERN large hadron collider*. [S.l.]: Jinst, 2008. Cited 2 times in pages 16 and 29.
- 23 CMS Collaboration et al. The CMS experiment at the CERN LHC. *JInst*, v. 3, p. S08004, 2008. Cited 2 times in pages 16 and 29.
- 24 THOMSON, M. *Modern particle physics*. [S.l.]: Cambridge University Press, 2013. Cited in page 16.
- 25 CHRISTENSON, J. H. et al. Evidence for the  $2\pi$  decay of the  $K_2^0$  meson. *Physical Review Letters*, APS, v. 13, n. 4, p. 138, 1964. Cited in page 18.
- 26 WEINBERG, S. The U(1) problem. *Physical Review D*, APS, v. 11, n. 12, p. 3583, 1975. Cited in page 19.

- 27 SOZZI, M. *Discrete symmetries and CP violation: From experiment to theory*. [S.l.]: Oxford University Press, 2008. Cited in page 19.
- 28 BRANCO, G. C.; LAVOURA, L.; SILVA, J. P. *CP violation*. [S.l.]: Oxford University Press, 1999. Cited 2 times in pages 19 and 20.
- 29 CREWETHER, R. et al. Chiral estimate of the electric dipole moment of the neutron in quantum chromodynamics. *Physics Letters B*, Elsevier, v. 88, n. 1-2, p. 123–127, 1979. Cited in page 19.
- 30 ALTAREV, I. et al. New measurement of the electric dipole moment of the neutron. *Physics Letters B*, Elsevier, v. 276, n. 1-2, p. 242–246, 1992. Cited in page 20.
- 31 WEINBERG, S. A new light boson? *Physical Review Letters*, APS, v. 40, n. 4, p. 223, 1978. Cited in page 20.
- 32 WILCZEK, F. Problem of strong P and T invariance in the presence of instantons. *Physical Review Letters*, APS, v. 40, n. 5, p. 279, 1978. Cited in page 20.
- 33 DUFFY, L. D.; BIBBER, K. V. Axions as dark matter particles. *New Journal of Physics*, IOP Publishing, v. 11, n. 10, p. 105008, 2009. Cited in page 20.
- 34 NOMURA, Y.; THALER, J. Dark matter through the axion portal. *Physical Review D*, APS, v. 79, n. 7, p. 075008, 2009. Cited in page 20.
- 35 DAVIDSON, A.; WALI, K. C. Minimal flavor unification via multigenerational Peccei-Quinn symmetry. *Physical Review Letters*, APS, v. 48, n. 1, p. 11, 1982. Cited in page 20.
- 36 BELLAZZINI, B. et al. R-axion at colliders. *Physical Review Letters*, APS, v. 119, n. 14, p. 141804, 2017. Cited in page 20.
- 37 CACCIAPAGLIA, G. et al. Light scalars in composite Higgs models. *Frontiers in Physics*, Frontiers Media SA, v. 7, p. 22, 2019. Cited in page 21.
- 38 FREESE, K.; FRIEMAN, J. A.; OLINTO, A. V. Natural inflation with pseudo nambu-goldstone bosons. *Physical Review Letters*, APS, v. 65, n. 26, p. 3233, 1990. Cited in page 21.
- 39 BRANCO, G. C. et al. Theory and phenomenology of two-Higgs-doublet models. *Physics Reports*, Elsevier, v. 516, n. 1-2, p. 1–102, 2012. Cited in page 21.
- 40 RINGWALD, A. Searching for axions and ALPs from string theory. In: IOP PUBLISHING. *Journal of Physics: Conference Series*. [S.l.], 2014. v. 485, n. 1, p. 012013. Cited in page 21.
- 41 MARCIANO, W. et al. Contributions of axionlike particles to lepton dipole moments. *Physical Review D*, APS, v. 94, n. 11, p. 115033, 2016. Cited in page 21.

- 42 OHTA, R. et al. The Tokyo axion helioscope. *Nuclear Instruments and Methods in Physics Research Section A: Accelerators, Spectrometers, Detectors and Associated Equipment*, Elsevier, v. 670, p. 73–78, 2012. Cited in page 21.
- 43 IRASTORZA, I. G. et al. The CERN axion solar telescope (CAST): status and prospects. *Nuclear Physics B-Proceedings Supplements*, Elsevier, v. 114, p. 75–80, 2003. Cited in page 21.
- 44 KHATIWADA, R. et al. Axion dark matter experiment: Detailed design and operations. *Review of Scientific Instruments*, AIP Publishing, v. 92, n. 12, 2021. Cited in page 21.
- 45 KNAPEN, S. et al. Searching for axionlike particles with ultraperipheral heavy-ion collisions. *Physical Review Letters*, APS, v. 118, n. 17, p. 171801, 2017. Cited in page 23.
- 46 CHANG, J. H.; ESSIG, R.; MCDERMOTT, S. D. Supernova 1987A constraints on sub-GeV dark sectors, millicharged particles, the QCD axion, and an axion-like particle. *Journal of High Energy Physics*, Springer, v. 2018, n. 9, p. 1–45, 2018. Cited in page 24.
- 47 CADAMURO, D.; REDONDO, J. Cosmological bounds on pseudo Nambu-Goldstone bosons. *Journal of Cosmology and Astroparticle Physics*, IOP Publishing, v. 2012, n. 02, p. 032, 2012. Cited in page 24.
- 48 DÖBRICH, B. et al. ALPtraum: ALP production in proton beam dump experiments. *Journal of High Energy Physics*, Springer, v. 2016, n. 2, p. 1–27, 2016. Cited in page 24.
- 49 SANCHEZ, P. Search for production of invisible final states in single-photon decays of Upsilon (1S). *arXiv:1007.4646*, 2010. Cited in page 25.
- 50 OPAL collaboration ABBIENDI, G. et al. Multi-photon production in  $e^+ e^-$  collisions at  $\sqrt{s} = 181\text{--}209$  GeV. *arXiv preprint hep-ex/0210016*, 2002. Cited in page 25.
- 51 Belle II Collaboration ABUDINÉN, F. et al. Search for axionlike particles produced in  $e^+ e^-$  collisions at Belle II. *Physical Review Letters*, APS, v. 125, n. 16, p. 161806, 2020. Cited in page 25.
- 52 ALONI, D. et al. Photoproduction of axionlike particles. *Physical Review Letters*, APS, v. 123, n. 7, p. 071801, 2019. Cited in page 25.
- 53 AALTONEN, T. et al. First search for exotic Z boson decays into photons and neutral pions in hadron collisions. *Physical Review Letters*, APS, v. 112, n. 11, p. 111803, 2014. Cited in page 25.
- 54 ATLAS Collaboration AAD, G. et al. Search for short-and long-lived axion-like particles in  $H \rightarrow aa \rightarrow 4\gamma$  decays with the ATLAS experiment at the LHC. 2023. Cited in page 26.
- 55 EVANS, L.; BRYANT, P. LHC machine. JINST. *S08001*, 2008. Cited in page 28.

- 56 ALICE Collaboration AAMODT, K. et al. The ALICE experiment at the CERN LHC. *Journal of Instrumentation*, IOP Publishing, v. 3, n. 08, p. S08002, 2008. Cited in page 29.
- 57 LHCb Collaboration AAIJ, R. et al. Study of coherent charmonium production in ultra-peripheral lead-lead collisions. *JHEP*, v. 2306, p. 146, 2022. Cited 2 times in pages 39 and 55.
- 58 GROSS, E. LHC statistics for pedestrians. CERN, 2008. Cited 2 times in pages 40 and 42.
- 59 READ, A. L. Presentation of search results: the CLs technique. *Journal of Physics G: Nuclear and Particle Physics*, IOP Publishing, v. 28, n. 10, p. 2693, 2002. Cited in page 40.
- 60 KLEIN, J. R.; ROODMAN, A. Blind analysis in nuclear and particle physics. *Annu. Rev. Nucl. Part. Sci.*, Annual Reviews, v. 55, n. 1, p. 141–163, 2005. Cited 2 times in pages 40 and 50.
- 61 BARLOW, R. J. Practical statistics for particle physics. *arXiv:1905.12362*, 2019. Cited 2 times in pages 41 and 44.
- 62 READ, A. L. *Modified frequentist analysis of search results (the CLs method)*. [S.l.], 2000. Cited 2 times in pages 42 and 43.
- 63 KLEIN, S. R. et al. STARlight: a Monte Carlo simulation program for ultra-peripheral collisions of relativistic ions. *Computer Physics Communications*, Elsevier, v. 212, p. 258–268, 2017. Cited in page 49.
- 64 FERRO-LUZZI, M. Proposal for an absolute luminosity determination in colliding beam experiments using vertex detection of beam–gas interactions. *Nuclear Instruments and Methods in Physics Research Section A: Accelerators, Spectrometers, Detectors and Associated Equipment*, Elsevier, v. 553, n. 3, p. 388–399, 2005. Cited in page 51.
- 65 BARSCHEL, C. *Precision luminosity measurement at LHCb with beam-gas imaging*. Tese (Doutorado) — RWTH Aachen U., 2014. Cited in page 51.
- 66 PUNZI, G. Sensitivity of searches for new signals and its optimization. *arXiv preprint physics/0308063*, 2003. Cited in page 51.
- 67 TLimit Class Documentation. Accessed: 2024-08-26. Disponível em: <<https://root.cern.ch/doc/master/classTLimit.html>>. Cited in page 62.
- 68 CRANMER, K. et al. *HistFactory: A tool for creating statistical models for use with RooFit and RooStats*. [S.l.], 2012. Cited in page 63.
- 69 VERKERKE, W.; KIRKBY, D. The roofit toolkit for data modeling. In: *Statistical Problems in Particle Physics, Astrophysics and Cosmology*. [S.l.]: World Scientific, 2006. p. 186–189. Cited in page 63.
- 70 MONETA, L. et al. The roostats project. *arXiv preprint arXiv:1009.1003*, 2010. Cited in page 63.